Cape Peninsula
University of Technology

# IMPLEMENTATION OF A REVERBERATION CHAMBER FOR ELECTRO-MAGNETIC COMPATIBILITY MEASUREMENTS

**by**

**VERENA KASHIKUKA NAFTALI**

**Thesis submitted in fulfilment of the requirements for the degree**

**Master of Engineering: Electrical Engineering**

**in the Faculty of Engineering**

**at the Cape Peninsula University of Technology**

**Supervisor: Prof. R. Van Zyl**
**Co-supervisor: Dr. G. Orjubin**

**Bellville**

**July 2017**

## DECLARATION

I, Verena Kashikuka Naftali, declare that the content of this thesis represents my own unaided work, and that the thesis has not previously been submitted for academic examination towards any qualification. Furthermore, it represents my own opinions and not necessarily those of the Cape Peninsula University of Technology.

**Signed** **Date**

## ABSTRACT

This research project focuses on the implementation of a Reverberation Chamber (RC) by the transformation of an existing electromagnetically shielded room. The reverberation chamber is a kind of shielded room designed to create a statistically random internal electromagnetic environment. The reverberating environment makes it possible to obtain high field strengths from a relatively low input power. The electric fields in the chamber have to be stirred to achieve a statistically uniform field.

The first part of this thesis presents an overview of reverberation chamber principles and preliminary calculations are done: the lowest usable frequency is estimated to be close to 300 MHz from empirical criteria. Modelling of the statistical environment is then presented, where electromagnetic quantities are characterised by probability density functions (Gaussian, Rayleigh and exponential); correlation issues are also presented.

Measurements are performed in the frequency range of 800 MHz – 4 GHz, dictated by the antennas available for this research study. An investigation of cable losses is conducted, followed by a discussion on measurement accuracy.

Mechanical stirrers are designed and manufactured. Electromechanical components are selected based on the literature study. Measurements are obtained through an automated setup using MATLAB®.

To verify that the RC, with its in-house designed mechanical stirrers, is well-operated, the stirring ratio is experimentally determined. After this first test, an exhaustive investigation of probability density functions is conducted, taking into account correlation issues. Measurements show that the quality factor of the chamber is close to 2000 at 3 GHz, and that 60 independent stirrer positions at 4 GHz can be used for statistical analyses.

Finally, the uniformity test is performed with an improved accuracy using frequency stirring. In conclusion, the CPUT RC passes the validation procedure according to the IEC 61000-4-21 standard by generating the required field uniformity within the accepted uncertainty level.

## ACKNOWLEDGEMENTS

**I wish to thank:**

- The Almighty God, for giving me strength and courage through his grace, to complete my thesis.
- My family for the moral support and encouragement during my studies.
- Prof. Van Zyl for giving me this opportunity to study the RC.
- Dr. Orjubin for the support, guidance, patience and scientific excellence, and all the time spent with me. It really means a lot to me and truly learned a lot from you.
- Mechanical department (Ali) for the construction of the mechanical stirrers
- Mr. Mark Rossow, I could count you anytime.
- All my classmates for academic support, guidance and encouragement.
- My friends for moral support and motivation.

The financial assistance of the National Research Foundation, French South African Institute of Technology, ESKOM and Namibian Government Scholarship Training Program towards this research is acknowledged. Opinions expressed in this thesis and the conclusions arrived at, are those of the author, and are not necessarily to be attributed to the National Research Foundation, French South African Institute of Technology, ESKOM and Namibian Government Scholarship Training Program.

## DEDICATION

I dedicate this thesis to my parents (Kletus Naftali and Ester Nakanyala) as a token of gratitude for their continuous support, love, encouragement and patience. Dad and Mom, thank you for inspiring the importance of hard work and higher education, and allowing me to go this far with my studies.

I further dedicate this thesis to my siblings (Tomas Naftali, Eva Naftali, Kletus Naftali and Ester Naftali) - you all contributed to this work. May you also be motivated, encouraged and inspired to reach your dreams. Ultimately, I dedicate this work to the Almighty God.

## RESEARCH OUTPUTS

1. Naftali V.K., Van Zyl R., Implementation of a reverberation chamber electromagnetic compatibility test facility. Abstract presented at CPUT Postgraduate Conference 2013, Bellville, South Africa, 5 November 2013.

2. Operating reverberation chamber prototype.

3. Naftali V.K., Mvouezolo P., Orjubin G., Cost-effective conversion of a shielded room into a Reverberation Chamber. Paper submitted.

## TABLE OF CONTENTS

## LIST OF FIGURES

# LIST OF TABLES

# GLOSSARY

## Acronyms/Abbreviations

| | |
|---|---|
| AC | Anechoic Chamber |
| AUT | Antenna Under Test |
| CPUT | Cape Peninsula University of Technology |
| F'SATI | French South African Institute of Technology |
| DUT | Device Under Test |
| EM | Electromagnetic |
| EMC | Electromagnetic Compatibility |
| EMI | Electromagnetic Interference |
| IEC | International Electrotechnical Commission |
| LUF | Lowest Usable Frequency |
| OATS | Open Area Test Site |
| RC | Reverberation Chamber |
| RF | Radio Frequency |
| SAC | Semi-Anechoic Chamber |
| TEM | Transverse Electromagnetic |
| UHF | Ultra High Frequency |
| VNA | Vector Network Analyser |

# CHAPTER 1: INTRODUCTION

## 1.1 Introduction

Advances in technology have seen miniaturisation of various electrical and electronic devices and systems. This, in turn, has brought electromagnetic interference sources closer to their victims, thereby escalating the problem of electromagnetic incompatibility (Corona *et al*., 2002). Nanosatellites employ such miniaturised technology, therefore the various subsystems of the satellites require an Electromagnetic Compatibility (EMC) assessment.

### 1.1.1 CPUT/F'SATI space programme

F'SATI is a collaboration between French and South African Universities. It is a specialised academic and research unit within the Cape Peninsula University of Technology (CPUT), Tshwane University of Technology (TUT), Ecole Supérieure d'Ingénieurs en Electronique (ESIEE) and Université Paris-Est (UPEC). A dual Master's programme in satellite systems engineering is offered where students obtain a Master of Engineering in Electrical Engineering from CPUT, as well as a Master of Science in Electrical and Electronic Systems Engineering from ESIEE, Paris.

The research programme focuses on developing national human capital in space science and technology through the CubeSat platform. This environment gives students practical experience in satellite technology and develops engineers and technologists that will support the space industry in South Africa (Visser, 2009). Shown in Figure 1.1 is the first nanosatellite that was developed by CPUT students and staff; it is called TshepisoSAT, meaning "promise", and was launched on 21 November 2013.

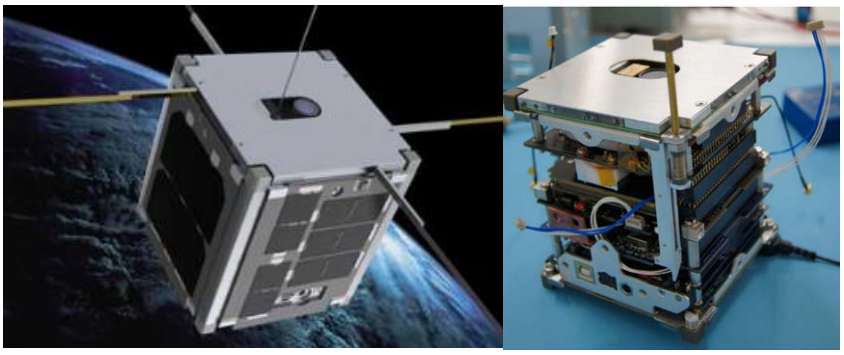

**Figure 1.1: The 1.2 kg ZACUBE-1 (TshepisoSAT) measuring 10 cm x 10 cm x 10 cm (From Visser, 2009)**

A one unit (1U) CubeSat is a satellite with a standard 10 cm × 10 cm × 10 cm form factor, and a mass of less than 1.3 kg (Wertz and Lanson, 1999). A 2U CubeSat is a stack of two 1U CubeSats and a 3U CubeSat is of three 1U CubeSats (Visser, 2009).

CubeSats are used for various applications, such as Earth Observation and space weather research. During the design process of CubeSats, technologies and techniques that reduce mass and power consumption without adversely affecting performance are applied. This increases the complexity of CubeSat hardware, which imposes strict design considerations on satellite reliability (Panetta *et al*., 1998). Qualification tests of satellites include thermal, vibration, radiation and electromagnetic compatibility.

F'SATI has developed a research program in the domain of EMC: the aim is to build an in-house EMC test facility to assess the EMC properties of CubeSats and/or subsystems.

The following section briefly describes the fundamentals of EMC analysis.

### 1.1.2 EMC concepts

Electromagnetic compatibility is defined as the ability of equipment to function satisfactorily in their electromagnetic environments without introducing intolerable disturbances into these environments or to other equipment. There are two aspects to EMC: Electromagnetic Interference (EMI) and Electromagnetic Susceptibility (EMS) (Montrose, 1994). Figure 1.2 represents the two parties (culprit and victim) that are involved in electromagnetic compatibility.

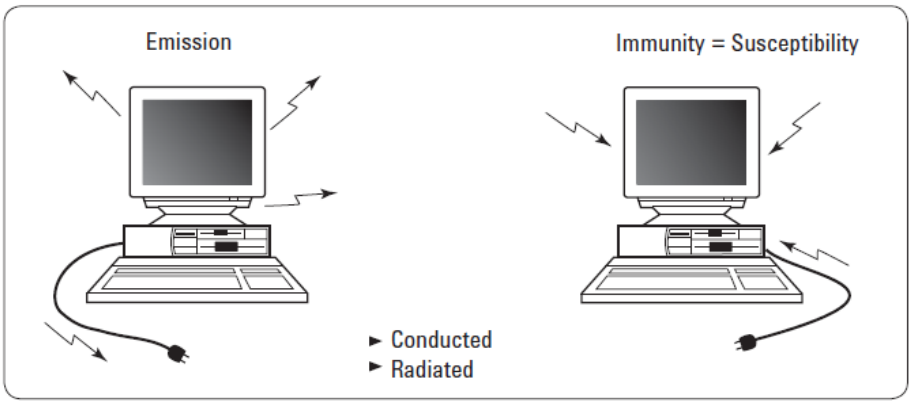


**Figure 1.2: Two parties involved in electromagnetic compatibility (From Sacchi, 2011)**

EMI is defined as electromagnetic energy emanating from one device, which causes another device to have degraded performance. Electromagnetic immunity/susceptibility is defined as the tolerance of devices in the presence of electromagnetic energy (Montrose, 1994). From an EMC perspective, in order to maximise compatibility, a product must be designed for two levels of performance: i) potentially interfering EM energy exiting (emissions), and ii) potentially interfering EM energy entering (susceptibility or immunity) an enclosure. Both emission and immunity can be associated with EM radiation and/or electrical conduction (Montrose, 1994: 1B-5).

To design electrical equipment that meets the EMC requirements, it is necessary to control the emission and reception of undesired electromagnetic energy by the equipment. This limiting, diverting, or absorbing of unwanted electromagnetic energy, also referred to as suppression, is accomplished at different design levels. These levels are: the board level, equipment interfaces, and enclosures.

EMI suppression at the circuit board level involves measures such as component selection, limiting signal bandwidth and transmission speed, board layout, and grounding practices (Clark *et al*., 1995:23). The equipment interface level is dominated by filtering and isolation, which are analogous to shielding techniques. Filtering and isolation limit the entry or exit of conducted EMI from equipment, whereas shielding limits the entry or exit of EM radiation.

### 1.1.3 EMC assessment of CubeSats

The F'SATI space programme requires an in-house facility for the EMC characterisation of its CubeSats and/or subsytems thereof. For this, it has been decided to equip the F'SATI laboratories with a Reverberation Chamber (RC), an EMC tool that has gained tremendous popularity over the past three decades (Besnier & Demoulin, 2011).

The following EMC tests can be performed with an RC (Laurence, 1998):

- Emission testing;
- Immunity testing; and
- Shielding effectiveness testing.

The range of applications is larger than EMC; RCs can also be used for antenna gain determination (Carlberg *et al*., 2005), emulation of a multipath environment (Genender *et al*., 2010), or measurement of the attenuation of connectors and cable shields (Warin, 1996).

## 1.2 Problem statement

A growing trend in nanosatellite missions is the use of highly integrated microelectronic devices. The proximity and density of the devices within the nanosatellite form factor give rise to the general problem of electromagnetic compatibility, which manifests itself as interference, susceptibility and electrostatic discharge. These phenomena may adversely affect the performance of the satellite itself and that of the launch vehicle.

Hosting a national nanosatellite development programme, F'SATI intends to ensure that its nanosatellites are electromagnetically compliant, whether the fields are self-generated or induced by an external source. Towards this goal, a shielded chamber has been upgraded to a reverberation chamber for electromagnetic compatibility tests. The reverberation chamber is fitted with so-called mechanical stirrers and electromechanical drivers. The behaviour of

the reverberation chamber has to be assessed and the uniformity of the internal field has to meet acceptable levels as required by the IEC 61000-4-21 standard.

### 1.3 Research questions

The aim of this study is to answer the following research questions:

- How can the existing screened room at CPUT be converted into an RC that meets the IEC 61000-4-21 acceptance standard?
- How is the quality factor impacted by the material used to construct the RC?
- How should the RC mechanical stirrers be designed?
- How can the measurements in the RC be automated?
- How do these stirrers generate a sufficient number of uncorrelated positions?
- How can the data sample size be increased using frequency stirring?

### 1.4 Objectives of the research

This research project focuses on an RC implementation by transforming an existing shielded room. The main objectives of this research are (1) to transform a shielded room into a reverberation chamber, and (2) to design, implement, characterise and calibrate the RC prototype in accordance with the IEC 61000-4-21 standard.

The specific objectives of the study are to:

- Develop stirrers that suit mode-tuned operation;
- Automate the EMC measurements procedure;
- Use an exhaustive set of criteria (i.e., stirring ratio, probability densityfunction, and field uniformity) to assess the RC behaviour;
- Use frequency stirring to improve the accuracy of the statistical characterisation of field uniformity.

### 1.5 Delineation of the research

This research focuses only on the mode-stirred technique. The CPUT RC will be equipped with two mechanical stirrers but only one is rotating. Operations with two stirrers will be studied in a future thesis. The measurement frequency range is from 800 MHz to 4 GHz and the electric field strength is measured with a short dipole. This is in agreement with the frequency range of available logarithmic compact antennas at the disposal of the project. Application of the constructed RC to perform EMC tests on a CubeSat is not investigated.

### 1.6 Significance of the research

The principal significance of having a calibrated reverberation chamber with an automated measurement setup is the ability to perform EMC characterisation of the F'SATI Cubesats

and subsystems in-house. This will ultimately improve the reliability and performance of their Cubesat missions.

### 1.7 Expected outcomes, results and contributions of the research

The following outcomes or results are expected from this research:

- Construction of an RC;
- Automated EMC testing interface;
- Verification of the RC;
- Thesis; and
- Research publication.

### 1.8 Thesis outline

The theoretical background and basic foundation of RCs are introduced in Chapter 2. Chapter 3 deals with electromagnetic fields inside a rectangular cavity. Chapter 4 focuses on statistical electromagnetics and probability distributions of EM fields inside an RC. The design and construction of the electro-mechanics are presented in Chapter 5. Chapter 6 introduces the concept of measurement precision using a Vector Network Analyser (VNA). Chapter 7 presents the measurements for the RC with the mechanical stirrers placed inside the cavity. Results are compared to the theory presented in Chapters 3 and 4. Conclusions and recommendations are given in Chapter 8.

# CHAPTER 2: LITERATURE REVIEW

## 2.1 Introduction

A reverberation chamber, also known as a mode-stirred chamber, is a tool for electromagnetic compatibility testing and other electromagnetic investigations. The concept of the RC has been known for many years, dating back to the 1960's (Besnier & Demoulin, 2011). The initial focus was to measure the attenuation of connectors and cable shields, but it has expanded to include radiated emission, susceptibility and immunity testing, and measuring the shielding effectiveness of cables, connectors and enclosures (Corona *et al*., 2002:88). The use of reverberation chambers was driven by the military, automotive and aircraft industries. This remains largely the same today.

RC's have two main advantages. The first is the removal of time-consuming Device Under Test (DUT) orientation changes. The other advantage is high E-field strength which can be realized without high gain RF-amplifiers.

## 2.2 EMC facilities for radiation testing

There are different types of EMC facilities for radiated emission and susceptibility testing: namely, Open Area Test Sites (OATS), semi-anechoic shielded chambers, full-anechoic shielded chambers, Transverse Electromagnetic (TEM) cells, Vibrating Intrinsic Reverberation Chambers (VIRC), and Reverberation Chambers (RCs) (Wiles & Rodrique, 2010). Although this thesis focuses on RCs, the other test facilities are presented briefly.

### 2.2.1 Open Area Test Site

An Open Area Test Site (OATS) is costly to construct and its use is weather dependent. It consists of a large conducting ground plane in an area that is free from any obstruction and with negligible ambient electromagnetic noise (Coates, 2004). The DUT is positioned on a circular turntable (able to do a full revolution). The setup also features a receiving antenna with adjustable position. Figure 2.1 shows an OATS.

**Figure 2.1: Open Area Test Site for antenna calibration testing as per CISPR 16-1-4 and CISPR 16-1-5 using a welded steel ground plane (From ETS-Lindgen)**

The OATS is used as a reference site for RCs (Rajamani *et al*., 2009:303-308). However, RCs have advantages over OATS (Eser & Sevgi, 2010):

- OATS are subject to the environmental conditions, such as rain and humidity;
- Measurements are done in an open space that can be perturbed by external factors; this can affect the measured results, unlike RCs where measurements are done inside a screened room;
- The testing time for full compliance radiated emissions tests in RCs is reduced compared to the OATS.

### 2.2.2 Anechoic chamber

As the term “anechoic” suggests, an anechoic chamber (AC) is designed to suppress EM wave reflections inside the chamber. It mimics free space scenarios, such as for the OATS, and it is suitable for testing at very high frequencies (Wiles & Rodrique, 2010).

Depending on the purpose of the chamber, it can either be semi-anechoic or full-anechoic. The full-anechoic shielded chamber is an EMC test facility where all surfaces are covered with electromagnetically absorbent material, including the floor. The advantage of full-anechoic shielded chambers is mainly that reflections from the floor cannot occur. The semi-anechoic shielded chamber is a shielded room of which only the walls and ceiling are covered with absorbent material. The floor is a metal reflecting ground plane (Wiles & Rodrique, 2010). Figure 2.2 shows the anechoic chamber installed at the University of Stellenbosch.

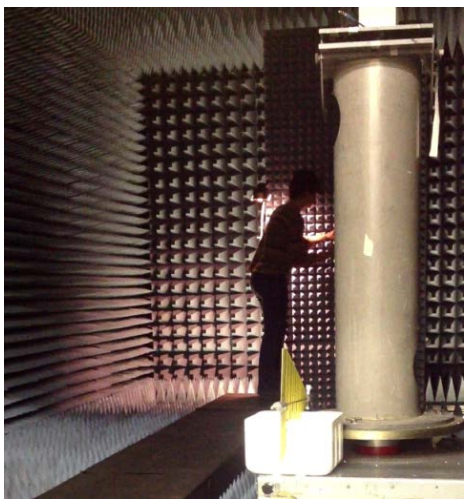

**Figure 2.2: Full-anechoic chamber at the University of Stellenbosch**

The disadvantages of an AC are that it has very high realisation costs. High gain amplifiers are used because ACs require higher input power than other test facilities in order to obtain a given field strength. The working volume inside the room is also reduced because of the thickness of the absorptive panels.

### 2.2.3 Transverse Electromagnetic cell

Transverse Electromagnetic (TEM) cells are also referred to as Crawford cells, which are named after its inventor (Pozar, 2005). TEM cells can be used for wide band EMC testing. It consists of a rectangular coaxial transmission section that is tapered on both ends, providing a uniform EM field distribution in a shielded environment (Nattaphong, 2008).

It is used to calibrate E-field broadband probes for testing radiated E-field immunity, as well as for measuring radiated emissions from products using a spectrum analyser or EMI receiver. TEM cells are compact and can match the performance of an OATS within the confines of a laboratory (Satav & Agarwal, 2008). Shown in Figure 2.3 is the transverse electromagnetic cell diagram.

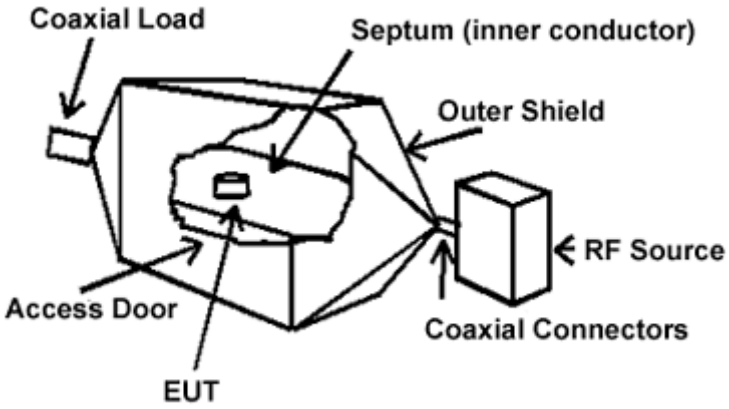


**Figure 2.3: Transverse Electromagnetic (TEM) cell diagram (Malaric, 2001)**

The Gigahertz Transversal Electromagnetic Mode (GTEM) cell is a TEM waveguide that has upper limits in the GHz range. A GTEM cell does not require antennas inside the cell itself, and therefore, no cabling that can affect the reproducibility of measurements adversely (Thye *et al*., 2009:592).

GTEM cells are immune to ambient noise conditions and measurement time is considerably shortened, compared to the measurement time taken at an OATS. For GTEM cells the field strength has to be measured in a vertical plane for a certain number of calibration points. Calibration is performed using electric field sensors, while the field strength is measured using network analysers accompanied by amplifiers (Satav & Agarwal, 2008). TEM cells used for immunity measurements must be tested for field uniformity and cross-polar coupling according to the IEC 61000-4-20 standard.

### 2.2.4 Reverberation Chamber

As stated earlier, a reverberation chamber is an EM shielded room with conductive mechanical paddles that are used to stir the inevitable standing waves that exist inside the

room. It is also known as a mode-stirred chamber, and it is used to perform EMC measurements (both emissions and immunity) of electronic equipment to determine compatibility with other electrical devices (Bäckstrőm *et al*., 2002:429).

A picture of the RC for the Electromagnetic Effect Research Laboratory (EMERL) at Nanyang Technological University, which is equipped with two mode stirrers, is shown in Figure 2.4.

**Figure 2.4: EMERL reverberation chamber for susceptibility measurements (From EMERL, 2007)**

The walls of an RC reflect radio frequency (RF) waves transmitted by antennas inside the chamber. The aim of an RC is to generate a statistically isotropic, randomly polarised and uniform electric field within an acceptable and predictable uncertainty and confidence limit. For this, the rotating mechanical stirrers inside an RC are used to change the cavity boundary conditions, thus modifying the field patterns. Averaging the multiple fields associated to the different stirrer positions leads to such a uniform and isotropic EM environment within the working volume. Isotropic means that fields at any given location within a working volume is the same in any direction.

Once the mechanical stirrers have rotated over a sufficient number of independent positions, the resulting field variations provide a set of field values involving many directions of propagation and polarisation. At any location, the local field shows large and irregular fluctuations during rotation due to varying levels of constructive or destructive interference of reflected waves from different spatial directions of incidence and polarisation at this location (Ladbury *et al*., 1999).

Research has been conducted in the past on the mechanical stirrer height, diameter and complexity (Coates *et al*., 2007:734-744). The number of independent stirrer positions that

can be achieved by a mechanical stirrer is still a subject of research (Pfenning & Krauthauser, 2013).

It has been shown that the RC represents a multipath environment similar to what is found in urban and indoor environments. The influence of multipath propagation on the bit error rate of a digital communication system can be investigated with an RC (Genender *et al*., 2010). As another application, radiation properties of antennas in a reverberating environment can also be measured with an RC (Carlberg *et al*., 2005).

An example of the commercial Bluetest RC800 RC is shown in Figure 2.5. This is a set up for radiated power measurements in this small cavity suited to study the EMC properties of cell phones. The field is stirred by two mechanical stirrers and by a source placed on a rotating platform (Bluetest, nd).

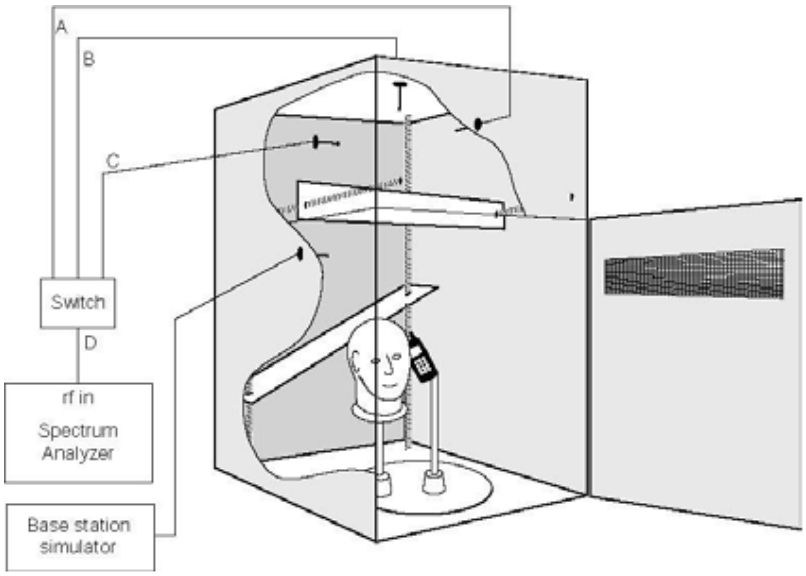


**Figure 2.5: Reverberation Chamber (From Bluetest.set®, nd)**

It has been seen that the enclosure boundary conditions can be changed using mechanical stirrers. An alternative way to mix the EM fields consists of operating a special stirrer-less cavity, called a Vibrating Intrinsic Reverberation Chamber (VIRC).

### 2.2.5 Vibrating Intrinsic Reverberation Chamber

The VIRC consists of a conductive cloth that forms the wall and a fan placed close to the wall to move or blow the walls in random directions. The random movement changes the boundary conditions inside the VIRC. Cavity modes are thus modified by the random movement of the RC walls, instead of using stirrers as in an RC (Leferink *et al*., 2000).

A picture of a VIRC is shown in Figure 2.6.

**Figure 2.6: Vibrating Intrinsic Reverberation Chamber (From Leferink, 2000)**

This approach does not get rid of mechanical problems associated with RCs completely, but removes the stirrers from the RC's interior. A VIRC only supports mode-stirred operation, and not mode-tuned operation. These modes of operation are described in the following section.

## 2.3 EMC testing methods in RCs

Mode-stirred and mode-tuned techniques are the two principal modes of operation of RCs (Besnier & Demoulin, 2011). Other operational modes that are often considered are the frequency stirring technique, which requires measurements at several close frequencies (Hill, 1994), and the source stirring technique, which uses a moving antenna instead of stirrers to stir the fields inside an RC (Bruns, 2005:64). These four techniques are presented next.

### 2.3.1 Mode-tuned technique

In mode-tuned operation, the stirrers are rotated by fixed steps with pauses between steps. Measurements (S-parameters or field strength obtained with a 3D probe) are taken at a single frequency whilst the stirrer is stationary. The sweep time is dependent on how long it takes for the electromagnetic fields to settle. This process is repeated over a full rotation of the paddles (Besnier & Demoulin, 2011:155), and eventually for a frequency sweep.

It is important to note that there is a minimum number of mechanical stirrer steps recommended by the IEC 61000-4-21 standard; e.g. a minimum of 50 steps is recommended at 1 GHz.

### 2.3.2 Mode-stirred technique

In this mode of operation, the stirrer rotates continuously with a uniform rotation speed. The collection of data is carried out at periodic time intervals.

Listed below are some technical considerations related to mode-stirred operations:

- The tuner can be rotated continuously with a gear reduction AC motor, and no stepper motor is necessary as for mode-tuned operation;
- The revolutions per minute of the tuner should be adjustable with different response times (typically 10-20 seconds/revolution);
- The dwell at each frequency is typically the time it takes for one full rotation of the tuner;
- This method requires chamber characterisation as per SAE J1113-27 (Besnier & Demoulin, 2011), with and without the DUT.

### 2.3.3 Frequency stirring technique

In the strict sense, frequency or electronic stirring of modes does not change the boundary conditions in an RC, but this operation comprises averaging the eigenfunctions over a narrow bandwidth (Hill, 1996). Practically, mode-tuned measurements are performed at different but close independent frequencies, and statistics are drawn from this hybrid set of measurements.

This technique will be employed in Chapter 7 to increase the accuracy of the statistical characterisation of field uniformity.

### 2.3.4 Source stirring technique

In order to stir the fields inside an RC, the source stirring technique uses a moving antenna (instead of moving stirrers). The source antenna is placed at several locations in the RC and its orientation is also changed. It yields the same characteristics as the mode-tuned technique. An advantage of using the source stirring technique is that there is no need for large stirrers inside the RC, resulting in a larger working volume. One limiting factor, however, is that it is only applicable to immunity testing (Bruns, 2005:64).

## 2.4 Experimental set up of an RC

A typical experimental RC set up for susceptibility testing consists of a DUT, a transmitting antenna driven by an RF amplifier or a VNA, and a computer to control the stirrers' displacement as illustrated in Figure 2.7.

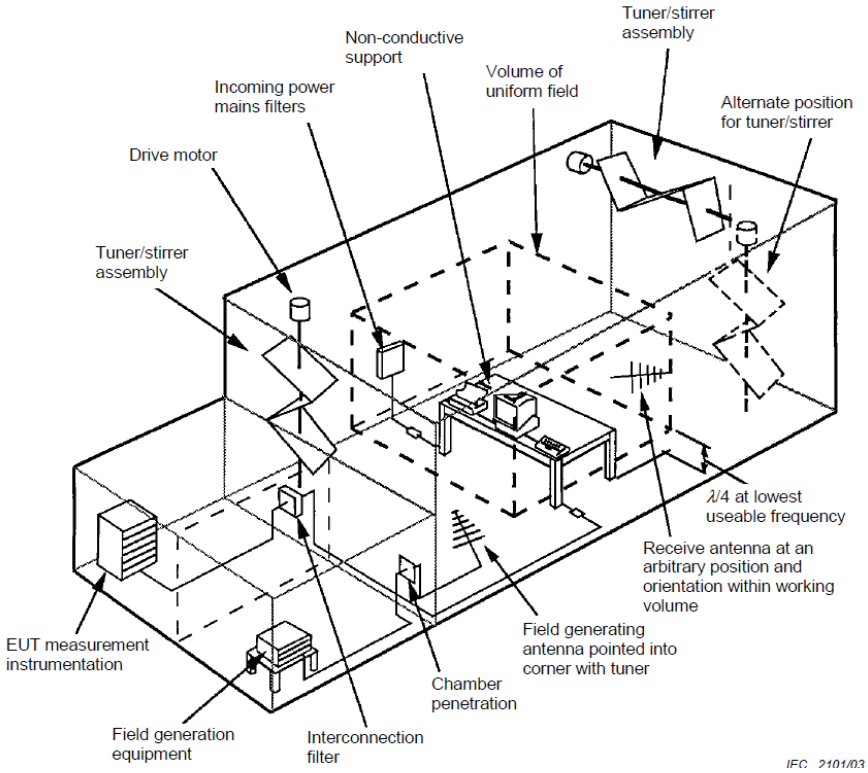


**Figure 2.7: A typical reverberation chamber facility (From IEC 61000-4-21 standard, 2009:35)**

According to the IEC 61000-4-21 standard, the DUT is placed anywhere in the working volume, which is a region defined by 8 points inside the chamber at quarter-wavelength distances ($\lambda/4$) from the walls to avoid boundary effects.

The field-generating antenna is pointed towards the corner of the chamber to eliminate direct coupling with the DUT. It should not illuminate the working volume or the receiving antenna and probes directly.

The E-field intensity can be derived from the power measured by a short dipole or directly measured with a 3-D probe. An amplifier must be used for susceptibility tests that require high field intensities.

Before any test is performed, one has to ensure that the RC is well-operated; this commissioning process is done through the acceptance test described in Section 2.5.

### 2.5 Acceptance testing standard for field uniformity

The acceptance testing standard uses field uniformity evaluation, which comprises a measurement of the maximum magnitude of the field strengths in the *x*, *y* and *z* directions at the 8 different positions defining the working volume. Figure 2.8 presents the chamber working volume.

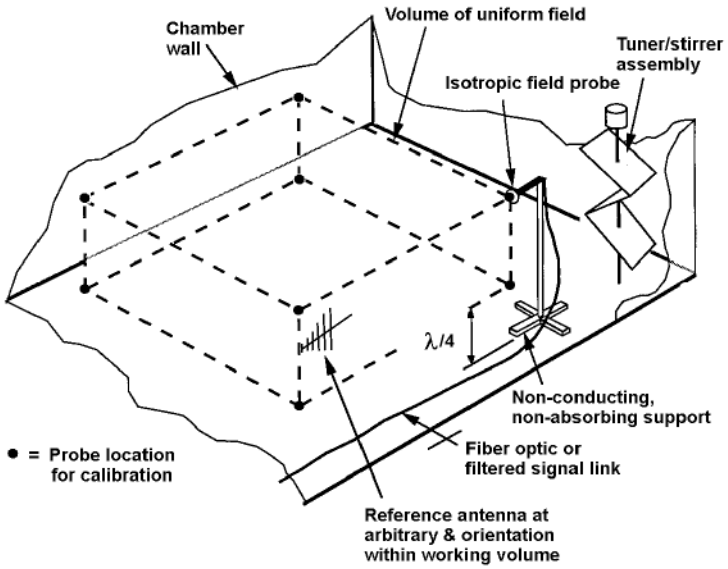


**Figure 2.8: Reverberation chamber working volume (From IEC 61000-4-21 standard, 2009:38)**

### 2.5.1 Calibration test

The steps below outline the calibration of an RC according to the IEC 61000-4-21 standard (Besnier & Demoulin, 2011).

1. The working volume should be cleared and a receiving antenna should be placed at a location within the working volume of the chamber.
2. The VNA is used to record $S_{21}$ measurements, which indicate how much of the incident power is transmitted to the receiving antenna. The frequency range should be set within the antenna frequency range and should be higher than the LUF.
3. In mode-tuned operation the stirrer is rotated through $N$ equally-sized discrete steps for a full revolution. Dwell time should be sufficiently long such that the VNA has enough time to respond correctly and the EM environment reaches steady state.
4. A probe or receiving antenna should measure the three components of the electric field.
5. This receiving antenna is then successively placed at the eight points defining the working volume.
6. For each frequency (of the VNA sweep) the data set corresponds to $N \times 8 \times 3$ complex values of $S_{21}$. These values of $S_{21}$ are related to field intensity $E$, in the three directions $x$, $y$ and $z$ as will be explained in Chapter 7.

The procedure to assess the field uniformity is described as follows:

1. For each antenna position, frequency and coordinate axis, determine the maximum value over the $N$ stirrer positions.
2. For each frequency, determine the standard deviation estimated from the eight locations and the three components.
3. Normalise this standard deviation using the mean value of the maximum.

4. Finally, the field uniformity is determined as the standard deviation $\sigma$ calculated from the dispersion of the normalised maximum values obtained at each of the eight locations during one rotation of the stirrer (IEC 61000-4-21, 2009).

The estimated standard deviation $\sigma$ of the RC is calculated as

$$\sigma = \sqrt{\frac{\sum_{i=1}^{n}\left(X_i - \overline{X}\right)^2}{n-1}}, \qquad \text{Equation 2.1}$$

where $n = 8 \times 3$, $X_i$ is the maximum electric field strength measured for each of the *x*, *y* and *z* axes, and $\overline{X} = \langle X \rangle$ is the mean value of these maxima.

This standard deviation is always expressed in dB relative to the mean using Equation 2.2:

$$\sigma_{dB} = 20\log\left(1 + \frac{\sigma}{\langle X \rangle}\right). \qquad \text{Equation 2.2}$$

The $X_i$ quantities should be expressed in linear scale, not in dB.

### 2.5.2 Acceptance testing standard

The IEC 61000-4-21 standard states that “The field within the chamber is considered uniform if the standard deviation is within 3 dB above 400 MHz, 4 dB at 100 MHz decreasing linearly to 3 dB at 400 MHz, and within 4 dB below 100 MHz. A maximum of three frequencies per octave may exceed the allowed standard deviation by an amount not to exceed 1 dB of the required tolerance”.

Figure 2.9 shows an example of standard deviation of probe data for a loaded chamber (IEC 61000-4-21).

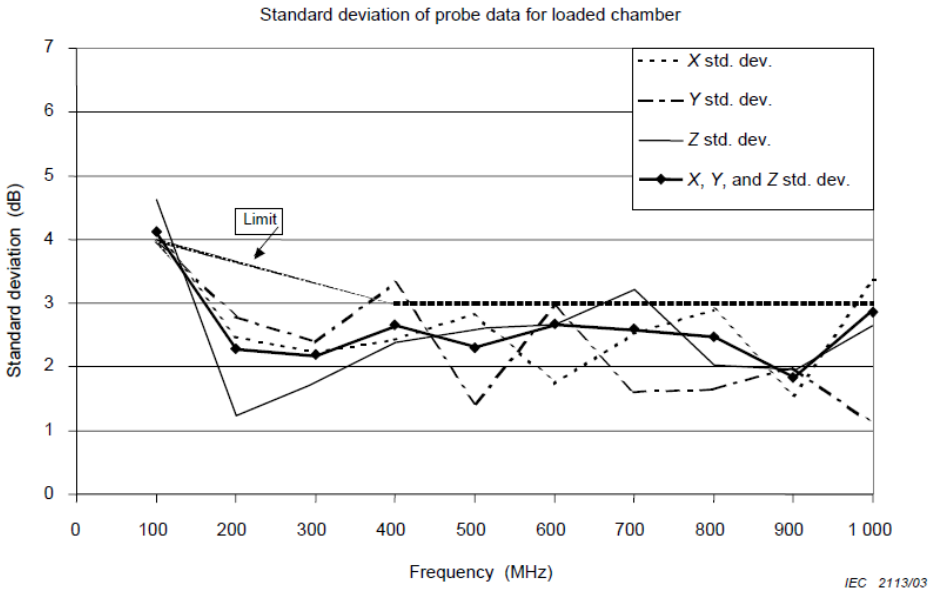


**Figure 2.9: Example of standard deviation of data for E-field components of 8 probes in the loaded chamber (From IEC 61000-4-21 standard, 2009:41)**

The standard deviation of probe data illustrated in Figure 2.9 is calculated using data from each axis independently and the total data set. This normalised standard deviation must fall within a 3 dB limit.

As already explained, a maximum of three frequencies per octave can exceed the allowed limit by an amount not exceeding 1 dB. Also, for frequencies lower than 100 MHz, the limit is modified as shown in Figure 2.9.

From the data shown in Figure 2.9, we can see that this RC is well-operated for frequencies higher than 100 MHz, as $\sigma_{\mathrm{dB}}$ is within the limits prescribed by IEC 61000-4-21 standard.

### 2.6 Summary

In this Chapter, different types of EMC test facilities were presented: namely, OATS, semi-anechoic shielded chambers, full-anechoic shielded chambers, TEM, VIRCs, and RCs.

Two principal modes of operation for RCs, namely mode-stirred and mode-tuned techniques, were discussed. Frequency stirring and source stirring techniques were also mentioned.

The acceptance testing standard for a reverberation chamber, based on field uniformity evaluation, was described.

# CHAPTER 3: ELECTROMAGNETIC FIELDS IN A RECTANGULAR CAVITY

In this chapter a rectangular cavity with Perfect Electrical Conducting (PEC) walls is analysed in order to understand the basic operating principles of the RC. In contrast to a stirrer-equipped cavity, a rectangular cavity has an analytical model that can be used to derive many properties of the actual RC, namely an estimation of the quality factor and the LUF.

## 3.1 Modal description of the chamber

Due to their resonating nature, fields of the lossless cavity can be expanded using modes.

### 3.1.1 Eigenmodes

Cavity modes are solutions of the propagation equation for lossless cavities without excitation. In its harmonic form, the equation to be solved is (Liu *et al.*, 1983)

$$\vec{\Delta}\,\vec{E} = -k^2\vec{E} \qquad \text{Equation 3.1}$$

with $k = \omega / c$ the wavenumber and $c$ the speed of light.

The boundary conditions are the following: the electric fields terminate normal to the conductor surface (the tangential component of the field must be zero) and the magnetic fields are tangential to the wall surface (the normal component of the magnetic field must be zero) (Pozar, 2005).

As Equation 3.1 is an eigen-equation of the Laplacian operator, a mode is also considered as an eigenvector, and its resonance frequency depends on the eigenvalue $-k^2$.

In the case of a rectangular cavity with PEC walls, Equation 3.1 is solved using a variable separation technique (Liu *et al*., 1983:6). It can be shown that the wave vector $\vec{k}$ must be quantified in each direction to meet the boundary conditions

$$\vec{k} = \begin{pmatrix} \frac{m\pi}{L_x} \\ \frac{n\pi}{L_y} \\ \frac{p\pi}{L_z} \end{pmatrix}, \qquad \text{Equation 3.2}$$

where $L_x, L_y,$ and $L_z$ are the dimensions of the cavity in the *x, y,* and *z* directions respectively, and *m, n,* and *p* are integers.

Consequently, the wavenumber can be written as

$$k_{mnp} = \sqrt{\left(\frac{m\pi}{L_x}\right)^2 + \left(\frac{n\pi}{L_y}\right)^2 + \left(\frac{p\pi}{L_z}\right)^2}\,. \qquad \text{Equation 3.3}$$

### 3.1.2 Resonant frequencies

From Equations 3.1, 3.2 and 3.3, the expression of the resonant frequencies are readily found:

$$f_{mnp} = \frac{c}{2}\sqrt{\left(\frac{m}{L_x}\right)^2 + \left(\frac{n}{L_y}\right)^2 + \left(\frac{p}{L_z}\right)^2}\,. \qquad \text{Equation 3.4}$$

These resonant frequencies can be sorted, bearing in mind that at least two integers must not be zero (Liu *et al.*, 1983). In our case, the cavity dimensions are $L_x \times L_y \times L_z = 1.86\ \mathrm{m} \times 2.47\ \mathrm{m} \times 2.44\ \mathrm{m}$. The lowest resonant frequency, also called the fundamental, is found to be:

$$f_{011} = \frac{c}{2}\sqrt{\left(\frac{1}{L_y}\right)^2 + \left(\frac{1}{L_z}\right)^2} = 86.4\ \mathrm{MHz}\,. \qquad \text{Equation 3.5}$$

### 3.1.3 Numerical study of the first modes

The analytically calculated results above apply to a rectangular stirrer-less cavity and therefore are not applicable to the RC equipped with a stirrer. A numerical simulation approach is useful to study the real RC but it has to be validated for the rectangular cavity. A simulation was done with CST Microwave Studio® to determine the first five modes. CST uses the time-domain Transmission-Line Matrix (TLM) method, which provides a full spectrum analysis using Fourier transforms (CST, 2013). Table 3.1 presents the first five resonant frequencies for the empty cavity simulated in CST, compared to the analytical results.

**Table 3.1: The first five modes for empty cavity**

| Mode number | Frequency (MHz) | | Indices ($m, n, p$) |
|---|---|---|---|
| | CST microwave | Theoretical | |
| 1 | 86.17 | 86.41 | 011 |
| 2 | 99.57 | 100.95 | 101 |
| 3 | 100.03 | 101.40 | 110 |
| 4 | 116.93 | 117.04 | 110 |
| 5 | 116.93 | 117.04 | 110 |

Good agreement is observed between this numerical approach and analytical results. This validation suggests that the real RC could be numerically studied at low frequencies. However, this particular numerical method is not suitable for high frequency analysis because the size of the mesh must be much smaller than the wavelength. This leads to a large scale problem requiring a large amount of CPU time and memory. Consequently, this numerical study was not taken further in this thesis.

### 3.1.4 Cumulated number of modes

One method for theoretical determination of the LUF is based on the cumulated number of modes.

The cumulated number of modes $N(f)$ with resonant frequency lower than a given frequency $f$ is calculated by counting all $(m,n,p)$ until $f = f_{mnp}$ is reached. At least two of the three indices are not equal to zero (Liu *et al*., 1983:15). For a stirrer-less rectangular cavity the number of modes can be calculated using Equation 3.6 (Arnaut, 2001):

$$N(f) = \frac{8\pi}{3} V \left(\frac{f}{c}\right)^3 - \left(L_x + L_y + L_z\right)\frac{f}{c} + \frac{1}{2} \qquad \text{Equation 3.6}$$

where $V = L_x L_y L_z$ is the volume of the cavity.

Equation 3.6 is also known as the generalised Weyl formula. Weyl's law describes the asymptotic behaviour of the counting function of the eigenvalues. Figure 3.1 presents the total number of modes calculated using Equation 3.6.

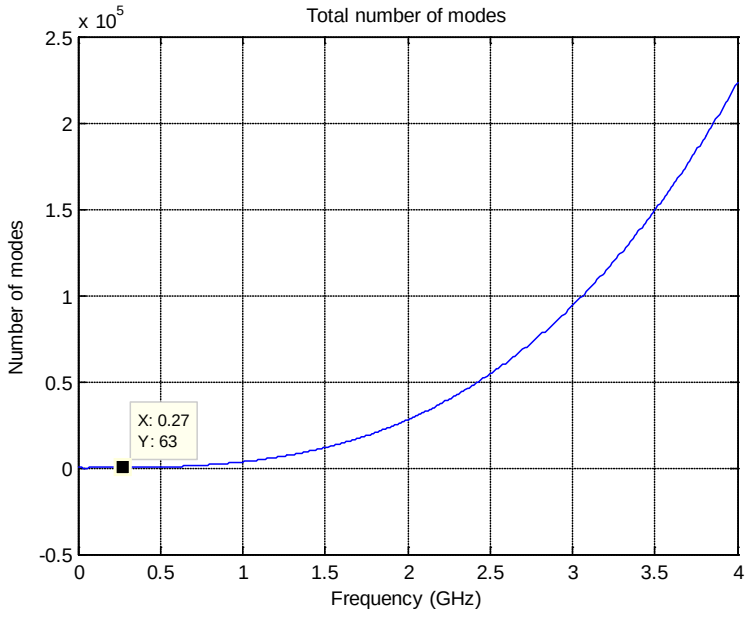


**Figure 3.1: Total number of modes using the generalised Weyl formula**

It is seen that at 3 GHz the cumulated number of modes is $10^5$. This justifies the denomination “overmoded cavity”.

Another interesting point is that at 270 MHz the total number of modes is 63. This information will be used in the next section.

Equation 3.6 is not an approximation and actually represents the smooth evolution with frequency of the number of modes. The so-called generalised Weyl formula is applicable not only for stirrer-less rectangular cavities, but also for the RC with stirrers as it is a chaotic system according to Orjubin *et al*. (2009:43).

### 3.1.5 Lowest Usable Frequency

According to the IEC 61000-4-21 standard, the LUF limit for a given chamber can be estimated using the following methods:

a) Find the frequency $f$ at which the total number of modes $N(f)$, given by Equation 3.6, is at least 60 modes.
b) Find the frequency that is three times above the first resonant frequency of the chamber, using Equation 3.5.
c) The LUF can also be experimentally found through a calibration procedure explained in Section 2.5, where a field uniformity criterion is determined from measurements at eight points. This method is not covered in this research study as the measurement frequency range is 800 MHz – 4 GHz.

The LUF obtained using the two methods described in a) and b) are listed in Table 3.2.

**Table 3.2: Lowest Usable Frequency for CPUT RC**

| Method | Frequency (MHz) |
|---|---|
| a) | 270 |
| b) | 258 |

The LUF from method (a) was determined using Equation 3.6, whereas the resonant frequency with indices $m = 0,\ n = 1,\ p = 1$ is used to determine the LUF using method (b).

In summary, the LUF of CPUT reverberation chamber is approximately 300 MHz.

## 3.2 EM fields in a well-operated RC

A well-operated RC is a cavity where the EM environment is assumed to be homogenous and isotropic. This is determined through a statistical process where a large number of samples of independent variables, such as stirrer position and frequencies, are considered.

EM quantities can then be considered as random variables mainly dependent on the stirrer position.

The ensemble average is noted as < >.

In the following sections, some formulas of practical interest are established using simple assumptions, such as isotropy and homogeneity of the EM field in a well-operated RC. These formulas are related to the square magnitude of the electric field $\left\langle |E|^2 \right\rangle$. It will be seen in Chapter 4 that the determination of the mean value of the electric field magnitude $\left\langle |E| \right\rangle$ (quantity measured with a sensor, not an antenna) requires some more assumptions.

### 3.2.1 Average power received by an antenna

The average power received $\langle P_R \rangle$ by an antenna is related to the mean value of the squared magnitude of the electric field $\left\langle |E|^2 \right\rangle$.

Using plane-wave integral representation for well-stirred fields in a reverberation chamber, Hill (1998) has given the expression of the mean power received by the antenna:

$$\langle P_R \rangle = \frac{1}{2} \langle S_C \rangle A_e \qquad \text{Equation 3.7}$$

where $A_e = \lambda^2 / 4\pi$ is the effective aperture area of an isotropic antenna, and $\langle S_C \rangle = c \cdot u$ is the average flux density of the plane wave. The $\frac{1}{2}$ factor is due to a polarisation mismatch (Ladbury *et al*., 1999:11). It can be noted that this expression is independent of the actual antenna gain.

The quantity $u$ is the average electromagnetic energy density of the total field (Ladbury *et al*., 1999:12),

$$u = \frac{1}{4}\left(\varepsilon_0 \left\langle |E|^2 \right\rangle + \mu_0 \left\langle |H|^2 \right\rangle\right). \qquad \text{Equation 3.8}$$

It can be proven that the average electric and magnetic energy densities are equal (Hill, 1998), property verified for lossless cavities:

$$u = \frac{1}{2}\varepsilon_0 \left\langle |E|^2 \right\rangle \text{ or } u = \frac{1}{2}\mu_0 \left\langle |H|^2 \right\rangle, \qquad \text{Equation 3.9}$$

with the permittivity $\varepsilon_0 = 8.85\times10^{-12}\,\mathrm{F/m}$ and the permeability $\mu_0 = 4\pi\times10^{-7}\mathrm{H}$ of the vacuum, respectively.

Substitution of Equation 3.7 gives

$$\langle P_R \rangle = c\varepsilon_0 \left\langle |E|^2 \right\rangle \frac{\lambda^2}{8\pi} \qquad \text{Equation 3.10}$$

which leads to

$$\left\langle |E|^2 \right\rangle = \frac{8\pi}{c\varepsilon_0\lambda^2}\langle P_R \rangle . \qquad \text{Equation 3.11}$$

As mentioned earlier, in a well-operated RC, it is assumed that the average electric field is isotropic and this implies that rectangular components of the electric field are equal,

$$\left\langle |E_{Rx}| \right\rangle = \left\langle |E_{Ry}| \right\rangle = \left\langle |E_{Rz}| \right\rangle = \left\langle |E_R| \right\rangle \qquad \text{Equation 3.12}$$

and also

$$\left\langle |E_{Rx}|^2 \right\rangle = \left\langle |E_{Ry}|^2 \right\rangle = \left\langle |E_{Rz}|^2 \right\rangle . \qquad \text{Equation 3.13}$$

As the three components have identical properties, it follows that,

$$\left\langle |E|^2 \right\rangle = 3\left\langle |E_R|^2 \right\rangle . \qquad \text{Equation 3.14}$$

Consequently, each “rectangular” component of the electric field is related to the received power, as described by

$$\left\langle |E_R|^2 \right\rangle = \frac{8\pi}{3c\varepsilon_0\lambda^2}\langle P_R \rangle . \qquad \text{Equation 3.15}$$

Substituting the wave impedance of free space $\eta_0 = \dfrac{1}{c\varepsilon_0} = 120\pi$ gives (Ladbury *et al*., 1999)

$$\left\langle |E_R|^2 \right\rangle = \frac{8\pi\eta_0}{3\lambda^2}\langle P_R \rangle = \frac{320\pi^2}{\lambda^2}\langle P_R \rangle . \qquad \text{Equation 3.16}$$

This formula is of great practical interest, as will be seen in Chapter 7.

### 3.2.2 Average power transmitted by an antenna

Before giving the expression of the RC gain in the next section, the power budget is first established.

The power transmitted by the transmitting antenna is $P_T$. In an ideal RC, the dielectric losses in absorbing materials (e.g. wood, carpet, wall coatings) and leakage can be ignored; the power budget is given by

$$\langle P_T \rangle = \langle P_W \rangle + \langle P_R \rangle \qquad \text{Equation 3.17}$$

where $P_R$ is the power received by the antenna, and $P_W$ is the total power dissipated in RC walls (and also in the stirrers). For high frequencies, the so-called plane-wave technique can be used to determine the expression of the EM fields (for any RC configuration). The average of the dissipated power $P_W$ has been given by Dunn (1990) is

$$\langle P_W \rangle = \frac{2\omega\delta\mu_r S}{3}\langle u \rangle, \qquad \text{Equation 3.18}$$

where $\mu_r$ is the relative permeability of the wall material, $S$ is the chamber surface area and $\delta$ denotes the skin depth of the material. This skin depth depends on the wall conductivity $\sigma_W$ and is calculated as (Pozar, 2009)

$$\delta = \frac{1}{\sqrt{\pi f \sigma_W \mu_0 \mu_r}}. \qquad \text{Equation 3.19}$$

If more than one receiving antenna is present, the average total power absorbed by all the antennas is simply the sum of powers absorbed by individual antennas. By superposition, the transmitting antenna also acts as a receiving antenna, unless an external control system is used to maintain a constant net power into the chamber (Ladbury *et al*., 1999:16).

Finally, from Equation 3.17 it follows that

$$\langle P_T \rangle = \frac{2\omega\delta\mu_r S}{3}\langle u \rangle + n\langle P_R \rangle \qquad \text{Equation 3.20}$$

where $n$ is the number of receiving antennas in the chamber. From this expression, the RC gain can be defined as described in the next section.

### 3.2.3 RC gain

The chamber gain $G$ is defined as the ratio of the average power received by an antenna to the average transmitted power:

$$G = \frac{\langle P_R \rangle}{\langle P_T \rangle}. \qquad \text{Equation 3.21}$$

Substituting Equation 3.20 into Equation 3.21 gives

$$\begin{aligned} G &= \frac{1}{n + 2\omega \dfrac{\delta \mu_r S}{3} \dfrac{\langle u \rangle}{\langle P_R \rangle}} \qquad \text{Equation 3.22} \\ &= \frac{1}{n + \dfrac{32\pi^2}{3} \delta \mu_r S \dfrac{1}{\lambda^3}} \\ &= \frac{1}{n + \dfrac{32\pi^2}{3} \dfrac{\delta \mu_r S}{c^3} f^3}. \end{aligned}$$

Finally, Equation 3.22 can be written in the form

$$G(f) = \frac{1}{n + b f^{5/2}} \qquad \text{Equation 3.23}$$

where $b = \dfrac{32\pi^{3/2} S \sqrt{\mu_r}}{3c^3 \sqrt{\sigma_W \mu_0}}$ is a constant depending on the wall properties (surface $S$, conductivity $\sigma$, relative permeability $\mu_r$) and $n$ the total number of antennas.

As $\delta$ is proportional to $f^{-1/2}$ (see Equation 3.19), the RC gain decreases as $f^{-5/2}$ at high frequencies (Ladbury *et al*., 1999:17).

The quantity $G$ can be measured using a VNA. To prove it, the relations between the incident power $P_{inc}$ and the received and transmitted powers are recalled:

$$P_T = \left\langle 1 - \left| S_{11} \right|^2 \right\rangle \times P_{inc} \qquad \text{Equation 3.24}$$

$$P_R = \left\langle \left| S_{21} \right|^2 \right\rangle \times P_{inc} \qquad \text{Equation 3.25}$$

where $S_{11}$ is the reflection coefficient at port 1, and $S_{21}$ is the transmission coefficient from port 1 to port 2. More details are given in Chapter 6.

Therefore, the chamber gain can be written as

$$G = \frac{\left\langle \left| S_{21} \right|^2 \right\rangle}{1 - \left\langle \left| S_{11} \right|^2 \right\rangle}. \qquad \text{Equation 3.26}$$

Equation 3.26 shows that the chamber gain can be inferred from the VNA measurements.

As will be seen during measurements, $S_{11} \cong 0$, fact illustrating that antennas are well matched. Besides the fact that the cavity is highly resonant, the gain is very small because of the internal losses; this point will also be verified during measurements. In conclusion, the following approximation can be done:

$$G \cong \left\langle \left| S_{21} \right|^2 \right\rangle. \qquad \text{Equation 3.27}$$

### 3.2.4 Antenna impedance in a well-operated RC

An antenna has a reflection coefficient $\Gamma_{fs}$ in free space. This reflection coefficient is usually small (because the antenna is well matched over its bandwidth), but $\Gamma_{fs}$ is not necessarily close to zero in the following. When placing this antenna inside a cavity, this reflection coefficient is modified and is assumed to be given by (Kildal *et al*., 2002)

$$\Gamma_{ant} = \Gamma_{fs} + \Gamma_{RC}, \qquad \text{Equation 3.28}$$

where $\Gamma_{RC}$ is the contribution from the reverberating environment.

Taking the ensemble average, and assuming $\left\langle \Gamma_{RC} \right\rangle = 0$ for high frequencies, this gives

$$\left\langle \Gamma_{ant} \right\rangle = \Gamma_{fs}. \qquad \text{Equation 3.29}$$

The reflection coefficient of an antenna in free space is then equivalent to the ensemble average of reflection coefficient of an antenna inside a cavity. This property is illustrated in Chapter 6.

## 3.3 Quality factor for an empty cavity

### 3.3.1 General consideration

The quality factor $Q$ is defined as the ability of the chamber to store energy. It is an important performance parameter for the RC because it determines the field enhancement and the decay time (Ladbury *et al*., 1999:12).

An RC is a cavity with relatively few losses and its quality factor is generally higher than 1000 (Besnier, 2015). However, leakage can reduce the chamber quality factor significantly. Also, dissipative elements inside the chamber, for example a wooden floor, reduce the quality factor and should therefore be avoided (Hillgatner & Peier, 2005).

In order to achieve a high quality factor, high conductivity is needed, as the conductivity of the chamber walls contributes directly to the quality factor. However, if the quality factor is too high, it becomes more difficult to achieve a homogenous field distribution, especially in the low frequency range. Another disadvantage of a very high quality factor is an increase of the chamber time constant, which leads to longer relaxation times for pulse excitation. Hence, the quality factor should be optimised in order to achieve an acceptable compromise between input power requirements and chamber performance (Heinrich & Karsten, n.d).

There are different types of losses that can affect the quality factor:

- Loss due to power dissipated in the walls;
- Loss due to absorbing objects in the chamber;
- Leakage through apertures; and
- Loss due to the power dissipated in the load of the receiving antenna.

Another point must be raised: for practical experiments when the device is placed inside the chamber for testing, the volume, surface, and the surface resistance of the chamber change. This causes a modification of the loaded $Q$ and the resonant modes.

The total cavity quality factor is expressed as follows (Pozar, 2009),

$$Q = 2\pi \frac{W_s}{W_d} = 2\pi \frac{W_s}{P_d \times T} = \omega \frac{W_s}{P_d} \qquad \text{Equation 3.30}$$

where $\omega$ is the angular frequency, $W_s$ is the energy stored in the RC, $W_d$ is the energy dissipated during one period $T$ and $P_d$ is the power dissipated in the walls added to the power leaking through the receiving antenna. Recalling Equation 3.17, we have

$$P_d = P_T = P_W + P_R \qquad \text{Equation 3.31}$$

and consequently,

$$\frac{1}{Q} = \frac{P_T}{\omega W_S} = \frac{P_W}{\omega W_S} + \frac{P_R}{\omega W_S} \equiv \frac{1}{Q_W} + \frac{1}{Q_{Ant}}. \qquad \text{Equation 3.32}$$

It is worth noting that this composite quality factor can also include other kinds of losses.

### 3.3.2 Expression of $Q_W$ for a general cavity

To determine the expression of $Q_W$, we first determine the electromagnetic energy $W_s$ stored inside the RC. This energy can be expressed as

$$W_s = \iiint u \, dv \,. \qquad \text{Equation 3.33}$$

From Equation 3.9 the total energy $W_s$ is

$$W_s = \frac{1}{2}\iiint \varepsilon_0 \left\langle |E|^2 \right\rangle dv = \frac{1}{2}\iiint \mu_0 \left\langle |H|^2 \right\rangle dv \,. \qquad \text{Equation 3.34}$$

Using perturbation technique valid for low loss EM cavities (Ladbury *et al.* 1999), the power dissipated by Joule effect in the walls is

$$P_W = \frac{1}{2} R_s \oiint \left\langle |H_T|^2 \right\rangle dS \,, \qquad \text{Equation 3.35}$$

where $H_T$ is the tangential component of the magnetic field and $R_s$ is the surface resistance,

$$R_s = \frac{1}{\sigma_W \, \delta}. \qquad \text{Equation 3.36}$$

Substituting in Equation 3.30 yields

$$Q_W = \omega \frac{W_s}{P_W} = \frac{2\pi \, f \times \iiint \mu_0 |H|^2 dv}{R_s \oiint |H_T|^2 dS} \qquad \text{Equation 3.37}$$

$$= \frac{2\pi \, f \mu_0 \delta \sigma_W \iiint |H|^2 dv}{\oiint |H_T|^2 dS}$$

$$= 2\frac{\sqrt{\mu_0 \, \pi \, f \sigma_W}}{\mu_r} \times \frac{V}{S} \times h$$

$$= \frac{2}{\delta \mu_r} \times \frac{V}{S} \times h \,, \qquad \text{Equation 3.38}$$

where $V$ is the chamber volume, $\delta$ is the skin depth and $h$ is the form factor,

$$h = \frac{S}{V} \frac{\iiint |H|^2 dv}{\iint |H_T|^2 dS} \,. \qquad \text{Equation 3.39}$$

As this form factor is close to one, (Arnaut, 2003) varying from 0.7 and 1.4, Equation 3.38 is consistent with the following expression proved by Hill (1996) using plane wave decomposition, under the assumption of non-magnetic walls ($\mu_r = 1$):

$$Q_W = \frac{3V}{2\delta S}. \qquad \text{Equation 3.40}$$

Therefore, $Q_W$ varies with the square root of frequency: $Q_W \propto \sqrt{f}$, meaning that higher frequencies lead to a more resonant RC.

On the other hand, the power dissipated in the walls increases with frequency:

$$P_W = \frac{1}{2\sigma_W}\sqrt{\pi\mu_0\mu_r f\sigma_W} \times \oiint |H_T|^2 \, dS. \qquad \text{Equation 3.41}$$

Therefore, $P_W$ is proportional to the square root of frequency: $P_W \propto \sqrt{f}$.

In summary, higher frequencies cause more losses, but they improve the quality factor.

### 3.3.3 Expression of $Q_W$ for a rectangular cavity

For a rectangular RC, the local mean value of $Q_W$ is given by (Liu *et al*., 1983)

$$Q_W = \frac{3V}{2\delta S} \times \frac{1}{1 + \frac{3\pi}{8k}\left(\frac{1}{L_x} + \frac{1}{L_y} + \frac{1}{L_z}\right)}. \qquad \text{Equation 3.42}$$

At high frequency, $k = \omega / c$ is large so that this equation converges to Equation 3.40.

This dependence of the quality factor on frequency is plotted in Figure 3.2. As Equation 3.42 does not take into account losses other than Joule losses, a common practice is to consider a low conductivity supposed to model these other losses (Arnaut, 2003); in our case, the conductivity is assumed to be $\sigma_W = 10^5$ S/m.

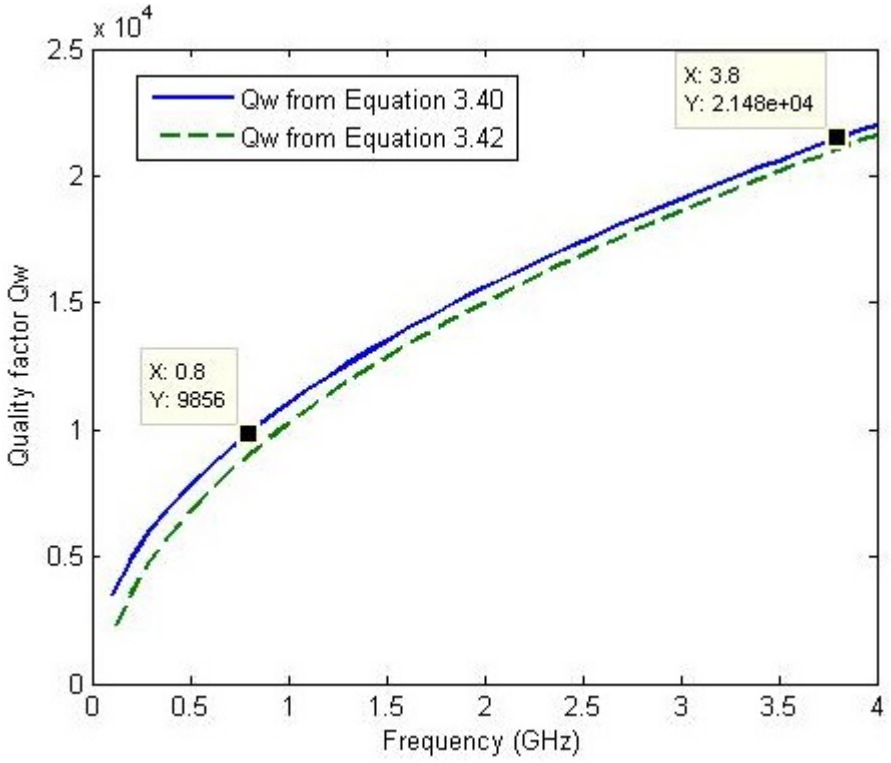


**Figure 3.2: Theoretical quality factor due to Joule effect in rectangular cavity**

For the frequency range between 800 MHz and 3.8 GHz, values are; $9.9\times10^{3}$ and $2.1\times10^{4}$. These values are comparable to the ones found in (Zhao, 2015) for a numerical simulation.

This preliminary estimation of a quality factor is useful to predict the field strength level to be generated in the working volume of the RC.

### 3.3.4 Practical determination of Q-factor

From Equation 3.30, assuming that the energy density $u = \frac{W_S}{V}$ is uniform, it follows that the composite quality factor (that takes into account all the losses, inclusive the leakage through the antenna) is:

$$Q = \omega \frac{V < u >}{< P_T >} = \omega V \frac{< S_C >}{c < P_T >} = \omega V \frac{< P_R >}{\frac{\lambda^2}{8\pi} c < P_T >} = \frac{16\pi^2 V}{\lambda^3} \frac{< P_R >}{< P_T >} \quad \text{Equation 3.43}$$

.

This formula from Hill (1996) allows an easy experimental determination of the total quality factor $Q$ from the averaged power received by an antenna and the input power.

### 3.4 Summary

Fundamental concepts and key parameters of the RC were introduced in this Chapter. The RC is abstracted to a simple rectangular cavity to determine the quality factor and cumulated number of modes.

Using two empirical criteria, the LUF of the CPUT RC was estimated to be approximately 300 MHz.

Methods for derivation of the quality factor were established.

These parameters are important because they have a direct influence on the field uniformity within the chamber.

# CHAPTER 4: STATISTICAL ELECTROMAGNETIC ANALYSIS OF A REVERBERATION CHAMBER

## 4.1 Introduction

This chapter focuses on the derivation of the probability distribution of EM quantities. As explained in Section 3.5, RC operation is based on statistical electromagnetism considering the ensemble of values corresponding to different RC configurations, mechanical stirrers (Crawford & Koepe, 1986), source position (Cerri *et al*., 2009) or frequency stirring (Hill, 1994).

## 4.2 Probability distribution of EM fields

There are different approaches to model an ideal RC environment. Two of the approaches are discussed here. The first approach is that an RC is considered as an EM cavity characterised by quasi-stationary fields present inside the resonant cavity. The second approach is the plane wave integral representation for fields based on the angular plane wave spectrum (Hill, 2005). For the second approach, the angular spectrum is modelled in a probabilistic way based on correlation assumptions inside the working volume of the RC. These two approaches show that for an ideal RC operating in the high frequency domain (wavelength very small compared to the RC dimensions), a probabilistic description is suitable to characterise EM fields (Musso, 2003:7).

### 4.2.1 Central Limit Theorem

The Central Limit Theorem (CLT) states that the sum of a sufficiently large number of independent and identically distributed random variables, each of them with a mean and variance, is approximately normally distributed (Papoulis and Pillai, 2002).

An important application of the CLT is the determination of the mean value $\overline{X}$ of a population from a sample of finite dimension $N$. A good estimator of $\overline{X}$ is the simple average $\langle x \rangle$:

$$\langle x \rangle = \frac{1}{N} \sum_{i=1}^{N} x_i \,. \qquad \text{Equation 4.1}$$

The CLT states that the distribution of this average value converges towards a normal (or Gaussian) law that depends on the mean value $\overline{X}$ and the dispersion of $X$, denoted $\sigma$:

$$\langle x \rangle = \frac{\sum x}{N} \rightarrow \text{Normal} \left( \overline{X}, \frac{\sigma}{\sqrt{N}} \right). \qquad \text{Equation 4.2}$$

For any given distribution, averaging $N$ values together does not alter the expected value, but the standard deviation is reduced by a factor of $\sqrt{N}$ (Ladbury *et al*., 1999:34).

### 4.2.2 Electric field components distribution

This section explains and shows that when the quadrature components of the field are independent, identical and normally distributed, it is then possible to determine the mean and maximum fields at any position in the chamber's working volume by measuring the fields at one single point.

First, we expand each component of the electric field into real and imaginary parts:

$$\begin{aligned} E_x &= E_{xr} + jE_{xi} \\ E_y &= E_{yr} + jE_{yi} \\ E_z &= E_{zr} + jE_{zi} \end{aligned} \qquad \text{Equation 4.3}$$

Any rectangular component $E_R = E_r + jE_i$ of the electric field is therefore a complex number.

For a well-operated RC, the real and imaginary parts of the three rectangular electric field components are normally distributed (Gaussian) and independent (Musso, 2003:8). This property is a direct consequence of the CLT.

The Probability Density Function (PDF) for a normal distribution with mean $\mu = 0$ is given by

$$f_X(x) = \frac{1}{\sigma\sqrt{2\pi}} \exp\left[-\frac{(x-\mu)^2}{2\sigma^2}\right] = \frac{1}{\sigma\sqrt{2\pi}} \exp\left[-\frac{x^2}{2\sigma^2}\right]. \qquad \text{Equation 4.4}$$

Now that real and imaginary parts of $E_R$ are known, the PDFs of the other quantities (e.g. $E_R$, $E_R^2$, $E_T$) can subsequently be determined.

For example,

$$E_R = \sqrt{E_r^2 + E_i^2} \text{ and } E_T = \sqrt{E_{xr}^2 + E_{xi}^2 + E_{yr}^2 + E_{yi}^2 + E_{zr}^2 + E_{zi}^2}. \qquad \text{Equation 4.5}$$

As each real and imaginary component is independent, identical and normally distributed, the resulting electric field magnitude is distributed according to the Chi-distribution with 2 and 6 degrees of freedom for $E_R$ and $E_T$, respectively.

The PDF of the total electric field magnitude $E_T$ is Chi-distributed and is expressed as

$$f_{\chi_6}(x) = \frac{x^5}{8\sigma^6}\exp\left[-\frac{x^2}{2\sigma^2}\right]. \qquad \text{Equation 4.6}$$

For the rectangular component $E_R$, this is a Chi-distribution with 2 DoF, which is also called the Rayleigh distribution

$$f_{\chi_2}(x) = \frac{x}{\sigma^2}\exp\left[-\frac{x^2}{2\sigma^2}\right]. \qquad \text{Equation 4.7}$$

We can now study the squared quantities,

$$E_R^2 = E_r^2 + E_i^2 \text{ and } E_T^2 = E_{xr}^2 + E_{xi}^2 + E_{yr}^2 + E_{yi}^2 + E_{zr}^2 + E_{zi}^2. \qquad \text{Equation 4.8}$$

As sums of squared independent normal laws, these quantities are distributed according to a Chi-squared distribution. For example, the PDF of $E_T^2$ (proportional to the EM power density) is

$$f_{\chi_6^2}(x) = \frac{x^2}{16\sigma^6}\exp\left[-\frac{x}{2\sigma^2}\right]. \qquad \text{Equation 4.9}$$

The discussed statistical considerations apply to both the electric and magnetic field within an RC and for the sake of simplicity this section only deals with the electric field.

Table 4.1 shows the summarised distributions for electric field amplitude and squared amplitude, power density and power received by an antenna (Musso, 2003:8).

**Table 4.1: Electric field probabilistic distributions inside an RC**

| EM quantity $x$ | Distribution | Probability function $f(x)$ | PDF *f*(*x*) |
|---|---|---|---|
| $\mathrm{Re}\{E_{x,y,z}\}$<br>$\mathrm{Im}\{E_{x,y,z}\}$ | Normal<br>Gaussian | $\frac{1}{\sigma\sqrt{2\pi}}\exp\left[-\frac{x^2}{2\sigma^2}\right]$ | 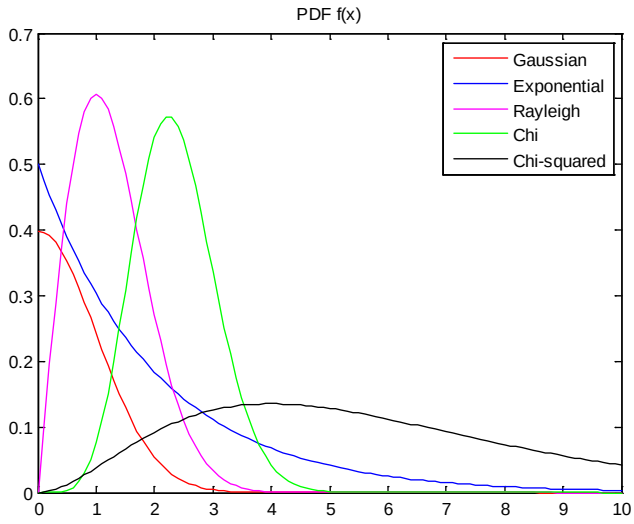 |
| $E_R = \lvert E_{x,y,z}\rvert$ | $x_2$<br>Rayleigh | $\frac{x}{\sigma^2}\exp\left[-\frac{x^2}{2\sigma^2}\right]$ | |
| $E_R^2 = \lvert E_{x,y,z}\rvert^2$ | $x_2^2$<br>Exponential | $\frac{1}{2\sigma^2}\exp\left[-\frac{x^2}{2\sigma^2}\right]$ | |
| $\lvert E_T\rvert$ | $x_6$<br>Chi | $\frac{x^5}{8\sigma^6}\exp\left[-\frac{x^2}{2\sigma^2}\right]$ | |
| $\lvert E_T\rvert^2$ | $x_6^2$<br>Chi-squared | $\frac{x^2}{16\sigma^6}\exp\left[-\frac{x}{2\sigma^2}\right]$. | |



These expressions are valid in a well-operated RC and comparisons of experimental distributions of these asymptotic curves are presented in Chapter 7.

There are two important points to be taken into consideration about transformations of random variables:

- Measurements are commonly presented on a logarithmic scale and one could be tempted to take the average of this value expressed in dB. This technique would result in an error because dB is not a linear operator, as stated in Equation 4.10:

$$\langle X \rangle_{dB} \neq \langle X_{dB} \rangle . \qquad \text{Equation 4.10}$$

- However, the differences are small for large samples $N > 100$ (Ladbury *et al*., 1999).

- Another example of this problem is related to the estimation of the mean value of a rectangular component $\langle E_R \rangle$. It could be tempting to use the expression $\left\langle |E_R|^2 \right\rangle = \frac{8\pi\eta_0}{3\lambda^2}\langle P_R \rangle = \frac{320\pi^2}{\lambda^2}\langle P_R \rangle$ from Section 3.2 and to take its square root.

  However, $\langle |E_R| \rangle \neq \sqrt{\left\langle |E_R|^2 \right\rangle}$.

The correct way to proceed is the following: determine the PDF of $E_R = \sqrt{E_r^2 + E_i^2}$ and then compute its expectation. It is known that $E_R$ is distributed as a Chi-function with two degrees of freedom, i.e., a Rayleigh distribution, and which expected value is

$$\langle E_R \rangle = \frac{\sqrt{\pi}}{2}\sqrt{\langle |E_R|^2 \rangle} = \frac{\pi}{\lambda}\sqrt{\frac{2}{3}\eta_0 < P_R >} = \frac{4\pi^{3/2}}{\lambda}\sqrt{5 < P_R >}. \qquad \text{Equation 4.11}$$

In summary, we have shown in this section how to determine the average $E_T, E_T^2, E_R$ from the measurements of the $P_R$ quantity.

Another application of this statistical modelling using PDFs is explained in the next section.

### 4.2.3 PDF of the maxima

Since the uniformity test procedure is based on statistics of maximum values, it is necessary to determine the PDF of these maxima.

If $N$ independent samples are taken from some known arbitrary distribution $X$, named the parent distribution, the theory of order statistics explains how to derive the PDF of the maximum of these samples (Ladbury *et al.*, 1999:34). We recall that the distributions $f_X$ of the parent quantities are defined in Table 4.1.

To define the PDF of a maximum, the Cumulated Distribution Function (CDF) of the parent distribution $X$ should first be determined and is defined as

$$F_X(x) = \text{Prob}(X < x), \qquad \text{Equation 4.12}$$

and the PDF is given by $f_X(x) = \frac{dF_X}{dx}$.

Let $\lceil X \rceil_N$ be the maximum among $N$ independent values; then according to the CDF definition,

$$F_{\lceil X \rceil_N}(x) = \text{Prob}(\lceil X \rceil_N < x)$$
$$= \text{Prob}\left(\max(X_1, X_2, X_3, ..., X_N) < x\right)$$
$$= \text{Prob}\ (X_1 < x \text{ and } X_2 < x, ..., X_N < x).$$

Assuming independence of the variables $X_k$, it follows that

$$F_{\lceil X \rceil_N}(x) = \text{Prob}\left(X_1 < x\right) \times \text{ Prob}\left(X_2 < x\right) \times \ldots \times \text{Prob}\left(X_N < x\right)$$

and since all the variables are identically distributed,

$$\begin{aligned} F_{\lceil X \rceil_N}(x) &= F_X(x) \times F_X(x) \times \ldots \times F_X(x) \\ &= F_X(x)^N . \end{aligned}$$

Therefore

$$F_{\lceil X \rceil_N} = F_X^N . \qquad \text{Equation 4.13}$$

This is the CDF for the maximum, knowing the distribution of the field.

Finally, the PDF for the maximum among $N$ samples can be derived as

$$f_{\lceil X \rceil_N}(x) = \frac{dF_X^N}{dx} = N\left[F_X(x)\right]^{N-1} \frac{dF_X}{dx} = N\left[F_X(x)\right]^{N-1} f_X(x). \qquad \text{Equation 4.14}$$

Applications of this general expression are given in the next section.

### 4.2.4 Maximum for Rayleigh and Exponential parent distributions

From Section 4.2.2, the power-related quantity $X = E_R^2$ is distributed exponentially

$$f_X(x) = \frac{1}{2\sigma^2} \exp\left[-\frac{x}{2\sigma^2}\right]. \qquad \text{Equation 4.15}$$

The parent CDF is, therefore, an exponential with $\mu = 2\sigma^2 > 0$, which is given as

$$F_X(x) = 1 - e^{(-x/\mu)} \qquad \text{with} \quad x > 0. \qquad \text{Equation 4.16}$$

Using Equation 4.13, the PDF of the maximum $\lceil X \rceil_N$ is derived as

$$f_{\lceil X \rceil_N}(x) = N\left[1 - \exp^{\left(-\frac{x}{2\sigma^2}\right)}\right]^{N-1} \frac{1}{2\sigma^2} \exp^{\left(-\frac{x}{2\sigma^2}\right)}. \qquad \text{Equation 4.17}$$

According to Papoulis and Pillai (2002), integral calculus leads to the expression of the expected value notated as $E\left[\lceil X \rceil_N\right]$ or $\left\langle E_{R_{\max}}^2 \right\rangle$:

$$\frac{\left\langle E_{R_{\max}}^2 \right\rangle}{\mu} = \sum_{i=1}^{N} \frac{1}{i} \cong 0.577 + \ln(N) + \frac{1}{2N}. \qquad \text{Equation 4.18}$$

Equation 4.18 is the ratio of the maximum power received by a wire antenna (over a stirrer rotation) to the mean power. According to Crawford (1981), the experimental values of this ratio are typically between 7 and 9 dB. This empirical value can be retrieved using Equation 4.18; for example, $N = 100$ leads to a ratio of 7.15 dB.

This property of the stirring ratio can be used to assess the behaviour of the RC (Ladbury *et al*., 1999).

Previous developments are useful to study the maximum power received by an antenna. In the case of data collected from an E-field sensor, the parent distribution $E_R$ is a Rayleigh distribution as shown in Table 4.1. A closed-form expression of the maximum of $E_R$ can be derived from Equation 4.14:

$$f_{\lceil E_R \rceil_N}(x) = N\left[1 - \exp^{-\frac{x^2}{2\sigma^2}}\right]^{N-1} \frac{x}{\sigma^2} \exp^{-\frac{x^2}{2\sigma^2}}. \qquad \text{Equation 4.19}$$

Contrary to the case of an exponential parent distribution, for a Rayleigh parent distribution the mean value of the maximum of the electric field does not have a closed-form expression and must be derived from approximations presented by Ladbury *et al*. (1999: 42).

### 4.3 Correlation study

The work presented in Section 4.2 assumes that samples are independent. Since each sample corresponds to an RC configuration at a given stirrer position, two consecutive stirrer positions should be uncorrelated and this condition is used to determine the maximum number of independent stirrer positions.

According to IEC 61000-4-21 standard, measurement data is regarded as uncorrelated when the correlation coefficient for increasing shifts drops below and remains less than the value of $1/e \approx 0.37$. As suggested by IEC 61000-4-21 (2009:23), the number of independent positions by dividing the total number of samples over one full rotation by the number of steps of the stirrer necessary to reduce the correlation coefficient to less than 0.37. This technique is called decimation and will be illustrated in Chapter 7.

The correlation coefficient between the two discrete ensembles $X$ and $Y$ with $N$ samples each can be calculated as (Ladbury *et al*., 1999)

$$\rho_{xy} = \frac{\frac{1}{N}\sum_{i=1}^{N}\left(x_i - \langle x \rangle\right)\left(y_i - \langle y \rangle\right)}{\sqrt{\sigma_x^2 \sigma_y^2}}, \qquad \text{Equation 4.20}$$

where $\sigma_X$ and $\sigma_Y$ are the dispersion of the ensembles $X$ and $Y$, respectively.

### 4.4 Ergodicity property

In the context of time series, ergodicity is the property of a random process for which time statistics of one sequence has the same properties as the ensemble of all the outcomes at a given time. In the case of an RC, three types of processes have ergodicity as property: spatial shift in the working volume, stirrer rotation, and frequency stirring. For frequency stirring, instead of using a tuner to change boundary conditions, the frequency is changed by some small amount (Musso, 2003:8). This technique will be used in Chapter 7 to increase the accuracy of estimations.

### 4.5 Summary

As a direct application of CLT, a fundamental property of a well-operated RC was established: the real and imaginary parts of the three electric field rectangular components are normally distributed and independent.

Classical transformations were applied to derive the PDFs and the first moment of EM quantities.

Order statistics were presented to model the distribution of the maxima. The expectation of the maxima of the electric field was expressed as a function of the number of independent stirrer positions.

The technique called *decimation* was presented: it is used to provide uncorrelated data.

# CHAPTER 5: DESIGN OF THE ELECTRO-MECHANICS

This chapter explains the design of the mechanical stirrers, the selection of the components, and the automation of the measurements.

## 5.1 Stirrer design – mechanical components

The mechanical stirrer is an essential part of the chamber design. It changes the boundary conditions of the EM field in order to generate a spatially homogenous field distribution inside the working volume of the chamber (Corona *et al*., 2002). This can either be done by a continuous rotation of the stirrer (stirred mode) or by stepping the stirrer in discrete steps (tuned mode). This research focuses on the latter.

There are different types of stirrers that have been designed and implemented worldwide, such as the Z-fold stirrer, and the fan-style stirrer. Figure 5.1 shows different types of stirrers.

(i)


(ii)

(iii)

(iv)

**Figure 5.1: Different types of stirrers : (i) Z-fold stirrers, (ii) triangular-base stirrer with perpendicularly mounted paddles, (iii) Rot-Z stirrer, a fan-style stirrer used in the RC of the Defence Science and Technology Organisation, Australia, and (iv) NPL rectangular stirrer**

Stirrers with relatively complicated structures exhibit higher performances than those which have a simple design (Corona *et al*., 2002). Positioning, orientation and structure determine the performance of stirrers within the RC.

A mechanical stirrer is constructed using metal, which can be aluminium for the benefit of light weight, or galvanised steel. It is installed with appropriate positioning equipment to allow the tuner to be rotated $360^{\circ}$ in evenly spaced increments. The size of the stirrer is directly related to its ability to change the electromagnetic field inside the chamber.

The stirrer should therefore be as large as possible with respect to the chamber size and wavelength at the lowest operating frequency. The stirrer design is important in the low frequency range to improve the field uniformity and to slightly lower the LUF (that is mainly determined by the cavity dimensions). Symmetries in the design of mechanical stirrers are avoided to maximise the number of independent positions that it can generate (IEC 61000-4-3, 2009:19). Figure 5.2 shows the dimensions of the mechanical stirrers designed and implemented in the RC at CPUT.

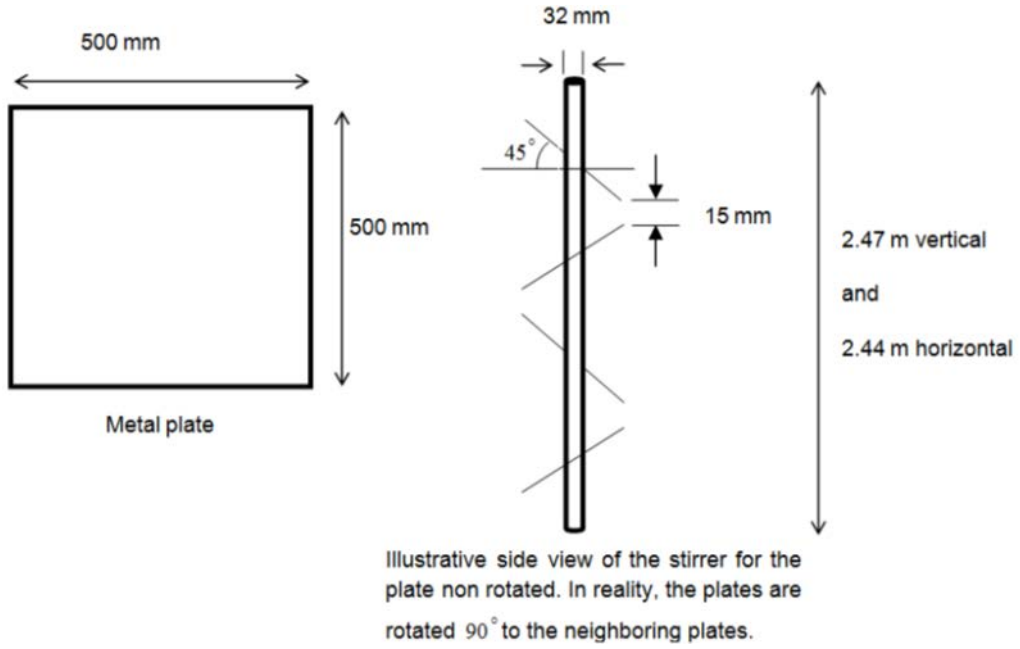


**Figure 5.2: Mechanical design of the stirrers of the CPUT RC**

There are four square plates with a side dimension of 50 cm fixed to a 32 mm diameter shaft. The plates are welded on supporting brackets that are fixed to the shaft with a slanting angle of $45^{\circ}$ and rotated $90^{\circ}$ to the neighbouring plates, but not touching each other. The distance between the lowest edges of the lowest paddle and the RC floor is 460 mm; this is the same for the distance between the top paddle and the ceiling.

The designed stirrers were constructed from galvanised steel. Galvanised steel was chosen since the machinery at CPUT's Mechanical Engineering Department cannot cut and weld aluminium. According to the IEC 61000-4-21 standard, the stirrer should have characteristic dimensions of at least $\lambda/4$ and extend at least over ¾ of the smallest chamber dimension. The size of the plates results from a trade-off between the stirrer and the working volumes. Moreover the side dimension of the square plates is equal to $\lambda/2$, leading to a resonance at 300 MHz that could slightly improve the LUF.

The implemented RC has two stirrers. One is mounted vertically in the corner opposite the door, and the other is placed horizontally across the chamber next to the door. Figure 5.3 shows these stirrers as viewed from the door. As stated in the thesis delineation, only the vertical stirrer will be rotating during measurements. The operation with two stirrers will be conducted in a future thesis where the improvement due to the second stirrer will be studied.

**Figure 5.3: Vertical and horizontal mechanical stirrers placed in the RC**

The following sections discuss the selection of stepper motor and driver, and the coupling between the stirrers and the stepper motor.

### 5.2 Stirrer design – electrical components

This section explains the basic setup of a stepper motor and all the blocks or components involved.

### 5.2.1 Basic stepper motor system setup

Figure 5.4 shows a typical stepper motor system. A schematic diagram of a complete stepping system is given in Appendix D.

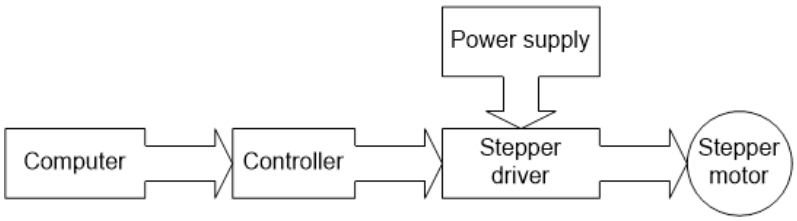


**Figure 5.4: Basic stepper motor system**

It is convenient to support the stirrer from the ceiling with the driver motor outside the chamber. The stirrers are driven by a stepper motor that is controlled with an Arduino Uno board (ATMEGA328P-PU microcontroller).

As will be discussed in Section 5.4.2, the stepper motor rotation is due to a current driven into the coil by a so-called stepper driver. This driver includes essential current limitation, and a pulse generator operating in both Pulse Width Modulation (PWM) and micro-stepping mode. It also determines the magnitude and direction of the current flow into the motor winding. The stepper driver receives commands from the controller that instructs the motor acceleration and velocity. The controller, in turn, is commanded from the computer with a high level language.

### 5.2.2 Selection of the stepper motor

A stepper motor creates rotation from current driven into its coils. It consists of a stator, a rotor with a shaft, and coil windings. The stator is a surrounding casing that remains stationary and is part of the motor housing. The rotor is a central shaft within the motor that actually spins during use (Hughes, 1993). Figure 5.5 shows a bipolar stepper motor.

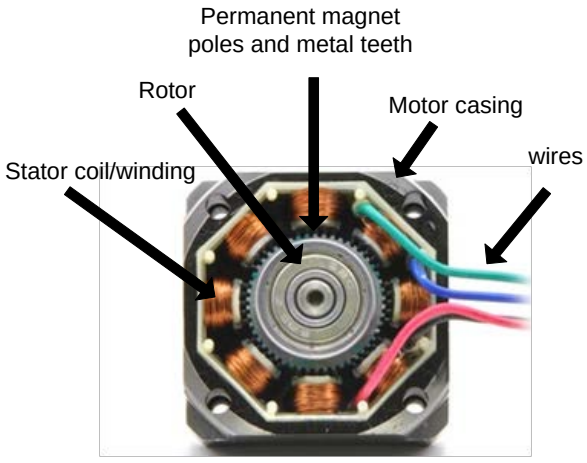


**Figure 5.5: Components of a bipolar stepper motor (From Grant, 2005)**

There are different types of stepper motors, namely, Permanent Magnet (PM), Variable Reluctance (VR), and Hybrid stepper motors. The PM motor creates rotation through the torque between a permanent magnet and an electromagnet created by electric current. When not powered, it exhibits some resistance to turning due to magnetic forces. The VR motor does not have a permanent magnet and creates rotation entirely with electromagnetic forces. It does not exhibit resistance to turning when the motor is not powered (Grant, 2005). The term Hybrid is derived from the fact that the motor is operated under the combined principles of the PM and VR stepper motors. Hybrid motors provide high resolution angular positioning and are good for applications requiring high repeatability and high torque in a small package size (Hughes, 1993).

The **hybrid-type** stepper motor is selected for this project as it provides a combination of the best features of both VR and PM types of stepper motors. The rotor for a hybrid stepper motor is multi-toothed, like the VR motor, and contains an axially magnetised concentric magnet around its shaft.

Stepper motors can further be categorised into bipolar or unipolar types. Bipolar stepper motors are composed of two windings and have four wires, whereas unipolar stepper motors have five or more wires. Unlike unipolar motors, bipolar motors have no centre taps, which is advantageous because the current runs through an entire winding, instead of just half of the winding. Thus, bipolar motors produce more torque than unipolar motors of the same size (Grant, 2005). The **bipolar motor** is selected due to its higher torque capability.

Figure 5.6 shows the wire connection diagrams for unipolar and bipolar stepper motors.

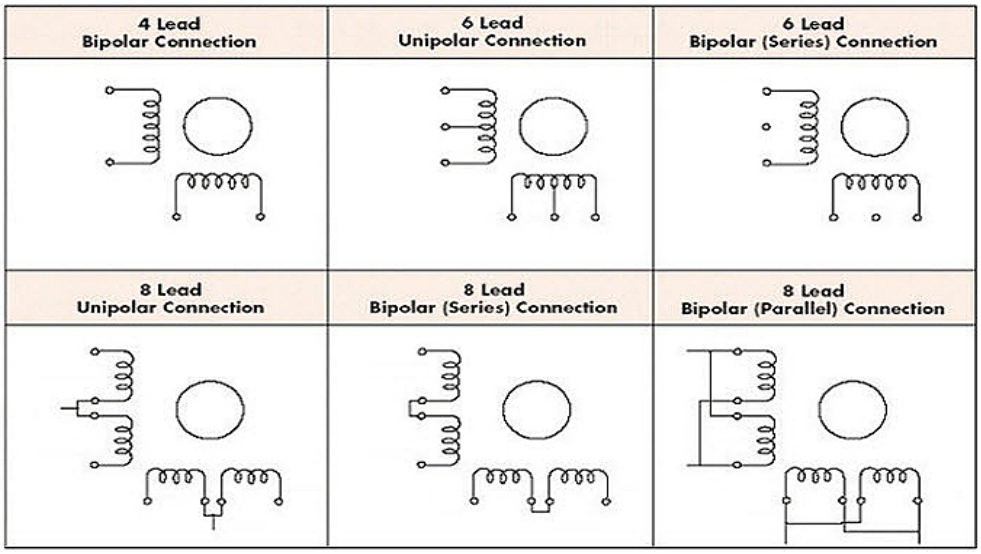


**Figure 5.6: Wire connection diagrams of unipolar and bipolar stepper motors (From Grant, 2005)**

In our case the 4 lead bipolar connections is used.

Two H-bridges are used to drive a bipolar stepper motor, as presented in Figure 5.7.

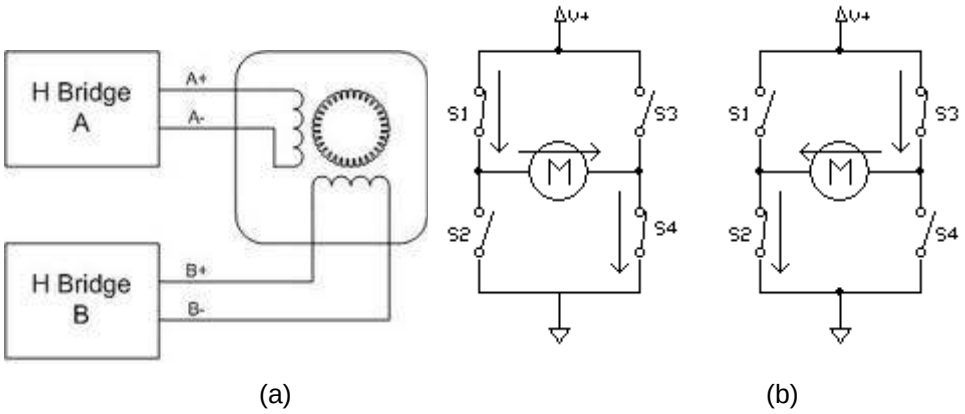


**Figure 5.7: (a) Four-wire bipolar stepper motor connected and (b) H-bridge circuits**

As stated above, a bipolar stepper motor has two windings, which are also known as phases. Each of the phases is connected to an H-bridge driver and the current can flow in both directions. As illustrated in Figure 5.7, the current flows from the positive rail of the power supply through one motor coil from the left to right and then to ground when S1 and S4 are closed. Current is driven in the opposite direction through the same motor coil when S3 and S2 are closed.

### 5.2.3 Determination of the holding torque

The most important parameter when selecting a stepper motor is the holding torque, which is determined by the stirrer characteristics and dynamics.

Another important parameter is the current rating, as the holding torque is proportional to the winding current. The voltage rating is derived from the motor rated current and winding resistance (Grant, 2005).

In order to estimate the torque required for the stepper motor, the following calculations are presented (Weeks, 2000).

#### i) Stirrer dynamics

To calculate the required torque *C*, the dynamics of a solid body in rotation around a fixed axis can be described by the approximated equation:

$$C = I \frac{\Delta \omega}{\Delta t} \qquad \text{Equation 5.1}$$

where $I$ is the moment of inertia and $\Delta \omega / \Delta t$ is the average angular acceleration during $\Delta t$.

This average angular acceleration is sketched in Figure 5.8.

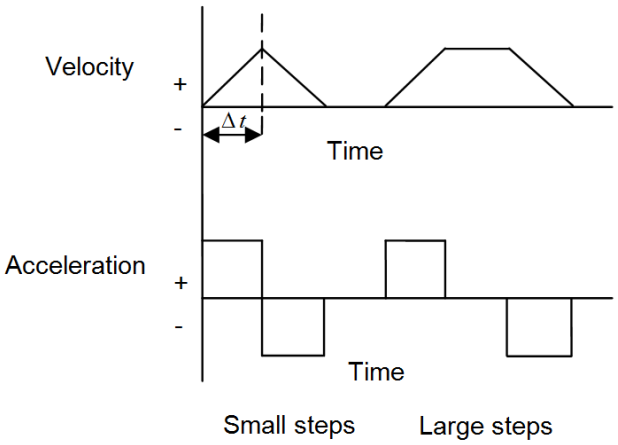


**Figure 5.8: Angular velocity and acceleration diagram**

Figure 5.8 gives an acceleration profile for tuned-mode operation, where the stirrer rotates in steps. It can be noted that acceleration is constant during $\Delta t$.

To estimate $\Delta t$, 200 steps per revolution (increments of 1.8 degree) are considered. Assuming that a full rotation is done in 400 s, the time between two consecutive steps is 2 s. The acceleration phase must be much smaller than 2 s. For subsequent calculations, $\Delta t = 0.2\,\mathrm{s}$ is chosen.

A maximum operating speed during the acceleration phase $\omega_{\max} = 1\ \mathrm{rpm}$ is considered. Thus, $\Delta\omega = \omega_{\max} - 0 = \ 2\pi / 60 = 0.1\ \mathrm{rad/s}$. Finally, the average angular acceleration is $\Delta\omega / \Delta t = 0.1 / 0.2 = 5\,\mathrm{rad/s^2}$.

To determine the torque required, the moment of inertia of the stirrer must be estimated.

### ii) Moment of inertia around a fixed axis

To determine the total moment of inertia $I = \sum mr^2$, the inertias of the shaft and of each plate are considered,

$$I_{Total} = I_{shaft} + 4I_{plate} \qquad \text{Equation 5.2}$$

where $I_{shaft}$ and $I_{plate}$ are the moments of inertia of the shaft and plate, respectively.

These quantities are calculated as follows (Hughes, 1993):

$$I_{shaft} = \frac{m_s}{12} 2\pi r^2 , \qquad \text{Equation 5.3}$$

$$I_{plate} = \frac{m}{12}(a^2 + 0.5a^2) , \qquad \text{Equation 5.4}$$

where $m_s$ and $r$ are the mass and the radius of the shaft, respectively, and *m* and *a* are the mass and the width of the rectangular shaped plate, respectively. Note that the plate inclination is 45 degrees, leading to a 0.5 coefficient for the effective height of the plate.

#### iii) Mass of each component

As shown in Figure 5.2, each plate has an area of $50\ \text{cm} \times 50\ \text{cm} = 2\ 500\ \text{cm}^2$ with a thickness of 1.9 mm. Galvanised steel density being 7 850 kg/m$^3$, each plate weighs 3.7 kg. The mass of the four plates for one stirrer is therefore 14.9 kg. Each stirrer features a centre tube (shaft) with a linear mass of 1.94 kg/m, and a length of 2.5 m, giving a total tube mass of $m_s$ = 4.85 kg. Finally, the total weight of each stirrer is 19.6 kg.

#### iv) Torque estimation

From Equations 5.1, 5.2, 5.3 and 5.4, the required torque is now determined as is $C \cong 3\,\text{Nm}$.

Figure 5.9 shows the high torque stepper motor used for this project. The selected stepper motor has a 2.8 A current rating and a 3.2 V voltage rating with torque of 1.9 Nm and step angle of 1.8 degree, see Appendix D for schematic diagram. This motor will be operated in micro-stepping mode.

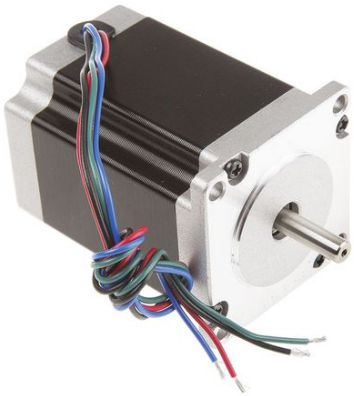

**Figure 5.9: Stepper motor 1.8°, 1.9 Nm, 3.2 V, 2.8 A, 4 wires selected for this project (From RS 535-0445)**

### 5.2.4 Stepper driver

The basic function of a motor driver is to provide the rated current to the motor windings in the shortest possible time (Grant, 2005). There are two commonly used drivers for stepper

motors; constant voltage drivers, also known as L/R or Resistance Limited (RL) drivers, and constant current drivers, also known as PWM drivers.

For a constant voltage driver, the driver current of the stepper motor is limited only by the resistance/impedance of its windings. With this driver it is important to match the motor's rated voltage to the voltage of the driver. It is inefficient at high speed and high current levels but works satisfactory at low speed and low current applications (Grant, 2005).

For constant current drivers (PWM) or chopper drivers, the motor current is regulated by switching the voltage of the motor on and off (chopping) to achieve an average level of current. These drivers operate using higher voltage supplies, generating higher driver voltage to motor voltage ratios for better performance at higher speed. This is the main advantage over the L/R drive (Grant, 2005). Due to these benefits, stepper motors are operated with bipolar chopper drivers at voltages higher than the rated voltages. For this project, a **PWM mode** driver is supplied with **20 V**, whereas the motor voltage rating is **3.2 V**.

Finally, a stepper motor can be driven in full-step, half-step or micro-step modes (Grant, 2005). In full-step mode, one digital pulse from the driver is equivalent to one step. This is achieved by energising both windings while reversing the current alternately. The motor produces full rated torque in this mode. As explained before, **micro-stepping** is used in this project. For additional information on half and micro-stepping controls, see Appendix A.

### 5.2.5 DQ542MA economical micro-stepping driver

A DQ542MA economical micro-stepping driver is selected. This is a 2-phase hybrid stepping motor driver, which uses advanced bipolar constant-current chopping techniques. Less motor heating is achieved by its 3 state current-control technology that allows coil currents to be well controlled with relatively small current ripple. The driver voltage is 18-50 VDC and the maximum phase current is 4 A. Schematic diagram of the driver is presented in Appendix D. Figure 5.10 shows a picture of the DQ542MA micro-stepping driver (Wantai, 2000).

**Figure 5.10: Micro-step driver DQ542MA (Wantai, 2000)**

The DQ542MA has two connectors: P1 for control signal connections and P2 for power and motor connections (Wantai, 2000). Appendices A and B provide more details about micro-stepping and PWM modes, respectively.

The maximum current is set to 2.8 A and the chopping frequency is 20 kHz (not adjustable).

The driver receives control signals from the Arduino Uno board (ATMEGA328P-PU microcontroller).

### 5.2.6 Stepper motor and stirrer coupling

A motor is typically connected to the load through a gear coupling. However, the selected motor associated to micro-stepping provides enough torque to suit the operation mode. So a direct coupling is adopted, although this simple technical solution requires attention to align the shafts. In our case, a piece of solid cylindrical metal provides the direct mechanical coupling. Figure 5.11 shows how this cylinder is coupled to the stirrer shaft though the bearings using epoxy glue.

**Figure 5.11: A solid cylindrical metal is glued to the stirrer shaft through the bearings; the stepper shaft is inserted at its other extremity**

## 5.3 Automated data acquisition

As presented in Section 5.2, an Arduino Uno board is used to control the driver. For full automation, the VNA is interfaced with the computer through MATLAB®, which in turn controls the Arduino Uno board.

Measurements for the reverberation chamber are automated as follows:

- Move the stirrer at a given position;
- Sweep the frequency;
- Select a channel associated with $S_{11}$ or $S_{21}$ and save the data on the PC;
- Create a 3D table containing measured data for all stirrer positions.

Figure 5.12 shows the flow chart for the automated measurements.

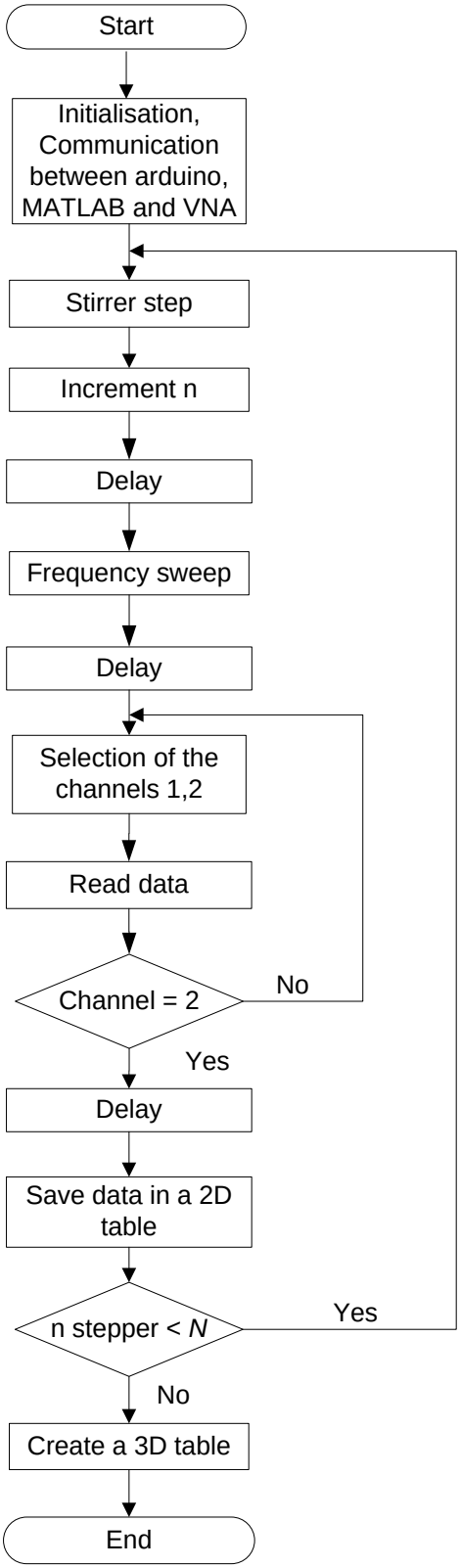


**Figure 5.12: Flow chart for automated data acquisition**

There are two main loops imbricated in increasing order of speed inwards: the outermost loop is associated with the stirrer rotation, the inner loop is associated with the frequency sweep, and is followed by a third loop that handles the change between channels. Measured data ( $f$, $S_{11}$, $S_{21}$) is then saved in a two-dimensional table. Post-processing begins with the

concatenation of these *N* tables (one table for each stirrer position) into a single three-dimensional table. The script can be found in Appendix C.

### 5.4 Summary

Mechanical stirrers were designed according to the IEC 61000-4-21 standard and constructed with galvanised steel metal. There are two mechanical stirrers in the CPUT RC, where one is placed vertically in the corner opposite the door and the other is placed horizontally across the chamber next to the door.

A bipolar hybrid-type stepper motor was selected for this project because it provides a combination of the best features of both VR and PM types of stepper motors. A bipolar stepper motor, furthermore, produces more torque than a unipolar motor. A brief mechanical study was done to estimate the required torque of the stepper motor directly coupled to the shaft. The selected motor has a current rating of 2.8 A and voltage rating of 3.2 V with torque of 1.9 Nm. The stirrer rotation is controlled through MATLAB® using an Arduino Uno board. A DQ542MA economical micro-stepping driver was selected. The flow chart of the fully automated RC measurements was presented.

# CHAPTER 6: MEASUREMENT PRECISION

This chapter covers experiments carried out to improve the accuracy of the measurements. This includes the VNA calibration procedure, cable loss measurement and modelling, and the determination of the correction factor.

## 6.1 Measurement setup

A VNA (Hewlett Packard 8720ET, 50 MHz to 20 GHz) is used to measure the S-parameters of the RC. The frequencies are swept between 800 MHz and 4 GHz using 1601 points. The incident power is 0 dBm.

For proper operation, a 4 s delay has been chosen to take into account the sweep time (0.8 s) of the VNA, the dwell time, as well as the time to transfer the data from the VNA to the computer. (See Appendix C).

Before any measurement is performed, the HP 85052D 3.5 mm economy calibration kit is used to calibrate the VNA. This is only done once and the setting saved.

Two HyperLOG® 7040 – Aaronia antennas are used as transmitting and receiving antennas connected to port 1 and port 2 of the VNA. Figure 6.1 illustrates the measurement setup.

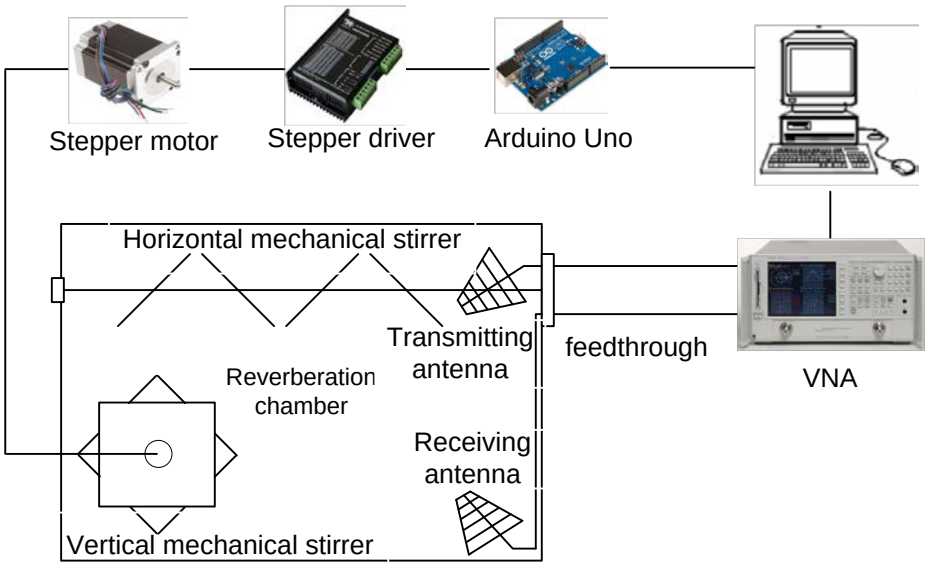


**Figure 6.1: Illustration of RC measurement setup**

The recorded data is saved to the computer from the VNA using a GPIB-USB cable through MATLAB® software. Connectors are tightened with the calibrated torque wrench.

Two calibrations are applied: the first one is a calibration in the plane of the antenna connections (inside the RC), and the second one is a calibration to the feedthrough plane.

Figure 6.2 shows the feedthrough panel that connects cables from the VNA to the antennas inside the cavity.

**Figure 6.2: Feedthrough cables**

The chamber is empty and contains only a transmitting and receiving antenna with feed cable lengths of 1 m and 6 m, respectively. Figure 6.3 shows the setup of the antennas inside the RC.

**Figure 6.3: Transmitting and receiving antennas inside the reverberation chamber**

The antennas are oriented orthogonally to minimize the cross-polarization. This does not appear clearly here because the two pictures in Figure 6.3 were taken at different angles.

### 6.2 Scattering parameters

According to Pozar (2005), scattering or S-parameters are the principal method to characterise linear microwave circuits and devices by using the concept of travelling waves.

The S-parameter description of a two-port network (see Figure 6.4) is presented here.

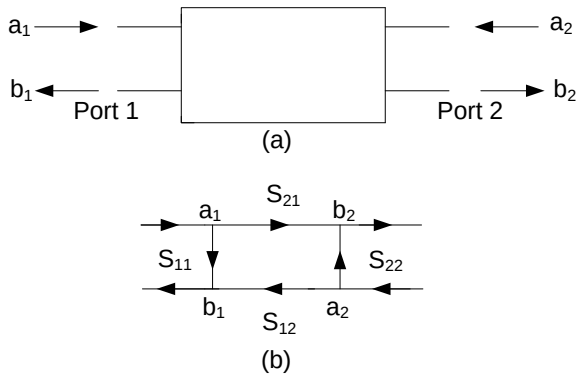


**Figure 6.4: Two-port network (a) schematic and (b) signal flow diagram (From Pozar, 2009)**

The formal definition of the S-parameters for a two-port device is given by (Pozar, 2009):

$$[B]=[S][A] \quad \text{or} \quad \begin{pmatrix} b_1 \\ b_2 \end{pmatrix} = \begin{pmatrix} S_{11} & S_{12} \\ S_{21} & S_{22} \end{pmatrix} \begin{pmatrix} a_1 \\ a_2 \end{pmatrix}. \qquad \text{Equation 6.1}$$

Quantities A and B are related to power; for example the incident power at port 1 is

$$P_1^+ = \frac{1}{2}|a_1|^2. \qquad \text{Equation 6.2}$$

The coefficient $S_{11}$ is the ratio of $b_1$ to $a_1$ if port 2 is terminated with a matched load (i.e. $a_2 = 0$). This is a special case of the input reflection coefficient $\Gamma_1$ at port 1, defined as the ratio of the amplitude of the reflected wave $b_1$ to the amplitude of the incident wave $a_1$ without necessarily ensuring that the output is matched.

The power $P_1^-$ reflected at port 1 is given by

$$P_1^- = \frac{1}{2}|b_1|^2 = |\Gamma_1|^2 P_1^+ \qquad \text{Equation 6.3}$$

and the total power at port 1 is

$$P_1 = P_1^+ \left(1 - |\Gamma_1|^2\right). \qquad \text{Equation 6.4}$$

The coefficient $S_{21}$ is the ratio of $b_2$ to $a_1$ when $a_2 = 0$. In the case of the RC, the $|S_{21}|^2$ measurement indicates how much incident power (that is transmitted by the transmitting antenna) is received by the receiving antenna. It is used to calculate the chamber gain,

defined in Section 3.7.3. The $S_{21}$ quantity is also used to study the EM distributions inside the RC (see Chapter 7). All measurements are done across the frequency range of interest.

Another quantity useful to characterize an antenna is the standing wave ratio (SWR) defined as

$$\mathrm{SWR} = \frac{1+|S_{11}|}{1-|S_{11}|} \qquad \text{Equation 6.5}$$

A perfectly matched antenna is characterized by SWR = 1.

## 6.3 Antenna measurements

### 6.3.1 Antenna outside the RC

The $S_{11}$ of the antenna is measured for the antenna placed outside from the RC and at 1m from any conductive material. Figure 6.5 illustrates the measured standing wave ratio (SWR) of the antenna placed outside the RC over its specified frequency range of 700 MHz - 4 GHz.

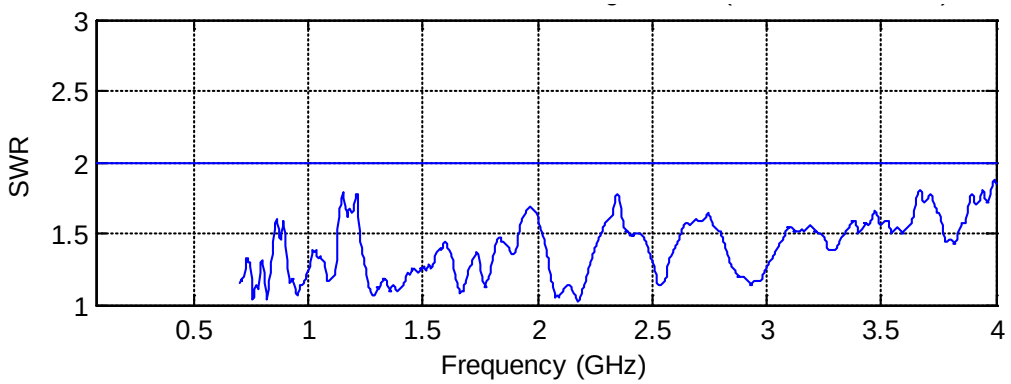


**Figure 6.5: Measured SWR of the antenna placed outside the chamber**

The SWR is lower than 2, which is in agreement with the published performance of this antenna (HyperLog ® 7040 X- Aaronia), see Appendix E.

### 6.3.2 Influence of the cables

The feeder cables inside the RC are long (6 m and 1 m) and therefore introduce losses into the measurements. To determine these losses, two $S_{21}$ calibrations are carried out; one at the plane of the feedthrough connectors, and the other at the plane of the antennas' connectors.

Figure 6.6 shows the comparison of $S_{21}$ for the two calibrations.

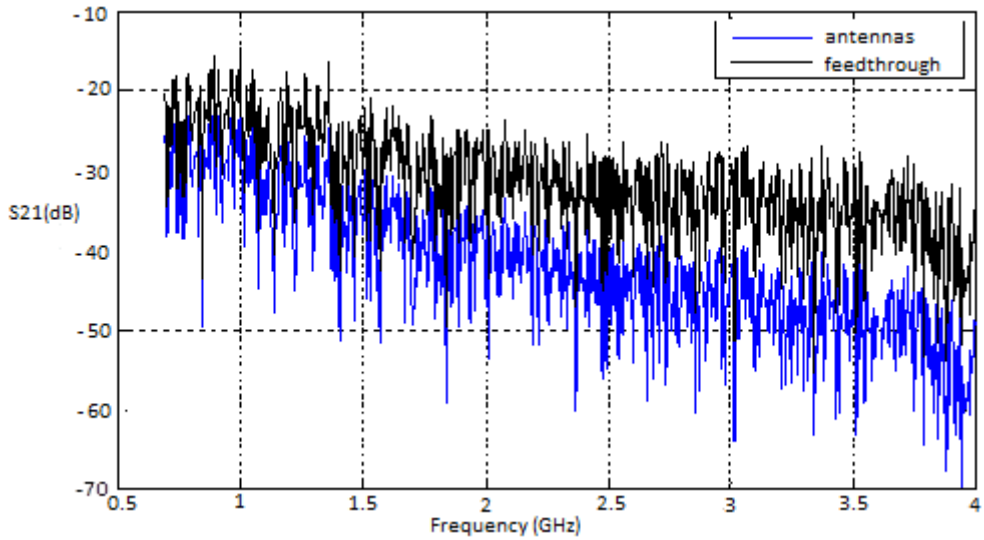


**Figure 6.6: Comparison of the $S_{21}$ response with 2 cables connections (calibration at feedthrough panel and at the antennas)**

The measured insertion loss for the calibration done at the feedthrough panel has fewer losses compared to the measured insertion loss for the calibration done at the antennas. Figure 6.6 shows that there is an attenuation ranging from -20 dB to -50 dB. The reasons for this large attenuation are multiple: losses of the RC, leakage of the RC, low quality of the cables. The latter attenuation can be compensated as shown further in this section. Figure 6.7 presents the difference of the two quantities shown in Figure 6.6.

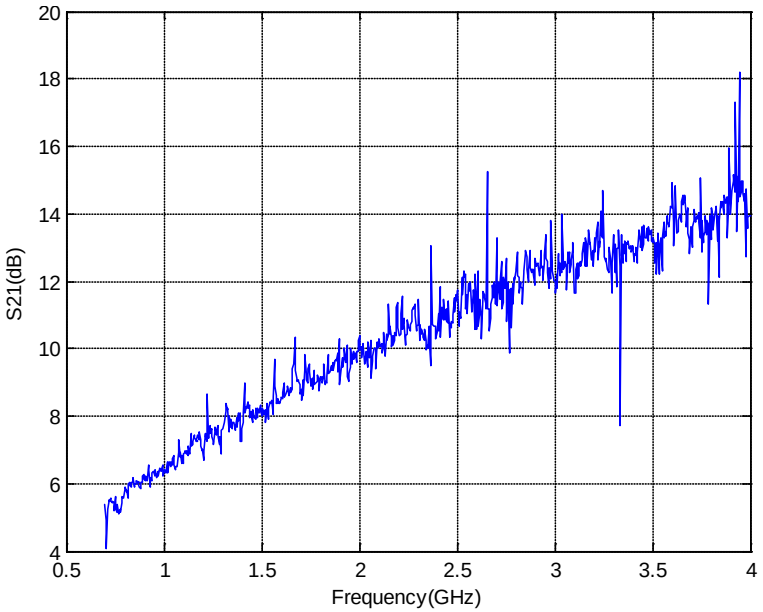


**Figure 6.7: Difference between the S-parameters represented in Figure 6.6**

In Figure 6.7, it is seen that the attenuation varies between 6 dB and 14 dB in the range of 700 MHz – 4 GHz. These values can be easily retrieved from a cable modelling. The datasheet gives the attenuation in dB for 100 m cable in a range of 0 – 1 GHz; this information is gathered in Figure 6.8.

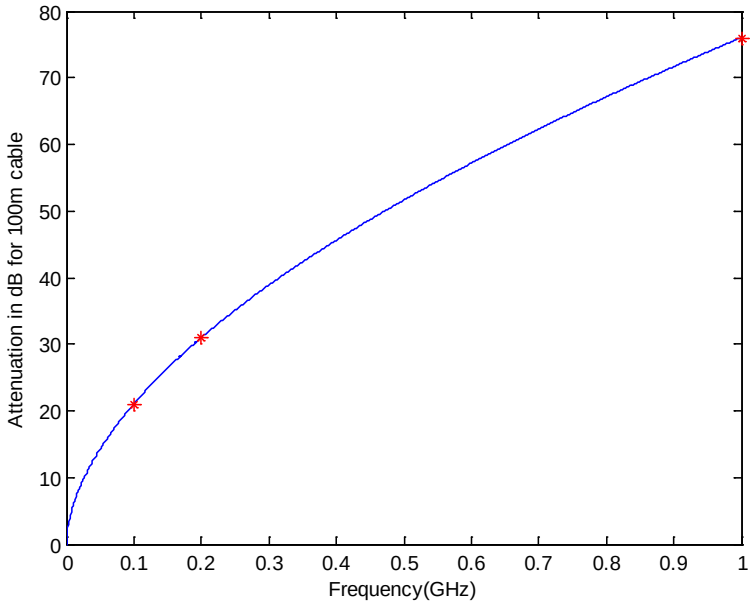


**Figure 6.8: Modelling of the cable losses obtained from the datasheet**

Figure 6.8 shows a curve fitting with power equation $\alpha_{fit} = a\, f^{\,b}$ and the matched results is obtained with $\alpha_{fit} = 7.24 \times f^{\,0.56}$. The exponential is close to 0.5, i.e., the theoretical value corresponding to Joule effect. The losses of the 7 m cable (1 m and 6 m for the transmitting and the receiving antenna, respectively) inside the chamber can now be predetermined from the previous model (Figure 6.8 plotted in green) obtained below 1 GHz. The comparison is presented in Figure 6.9.

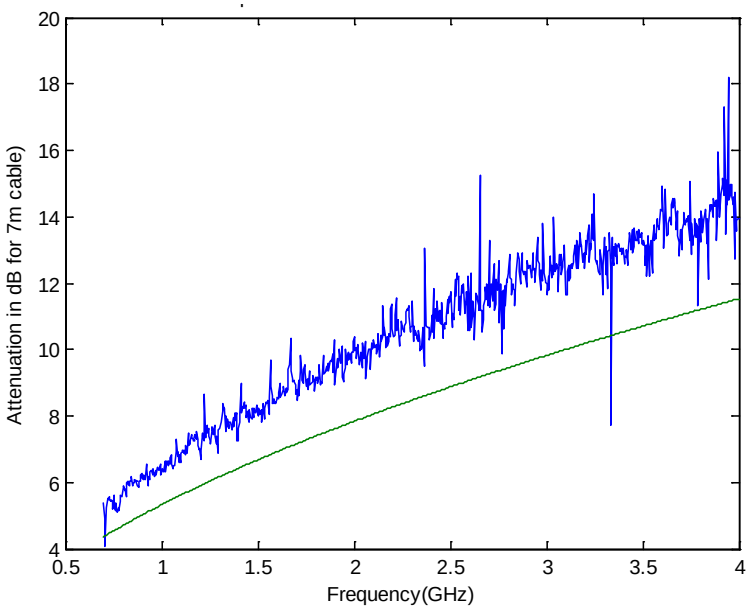


**Figure 6.9: Comparison of modelled and measured attenuation of the cables**

The experimental attenuation is higher than the predetermined one for various reasons:

- The two feedthroughs and the two connectors inside the RC induce losses of approximately 1 dB at 1 GHz.

- $\alpha_{fit}$ formula was obtained from the datasheet which range is only 0 - 1 GHz, whereas the measurements will be done in a range of 700 MHz - 4 GHz. This is a main issue because dielectric losses (proportional to $f$) are dominant at high frequencies.

In summary, the study shows that the feeder losses inside the RC can be compensated in order to estimate properly the $S_{21}$ of the RC. This is done by **calibrating the VNA at the antenna level**.

### 6.3.3 Antenna inside the RC

Now that the compensation is completed at the antenna level, comparison of SWR between the antenna in open space and the one inside the RC is made and presented in Figure 6.10.

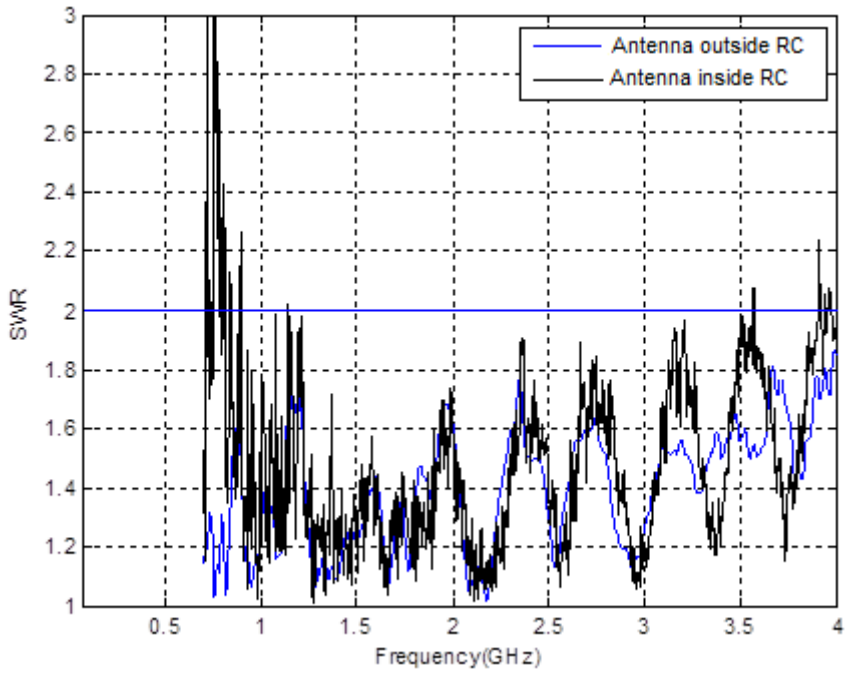


**Figure 6.10: SWR of the transmitting antenna inside and outside the RC**

Figure 6.10 shows that above 1.5 GHz, the SWR of the antenna inside the RC is similar to that of the antenna in open space. This property agrees with the theoretical analyses for a well-operated RC that is briefly explained in Section 3.7.4 (Ladbury *et al*., 1999:71, Kildal *et al*., 2002:113). To be more accurate, this technique requires that an average is done over many stirrer positions.

Figure 6.11 shows the comparison of $S_{11}$ for the antenna standing outside and the antenna inside RC.

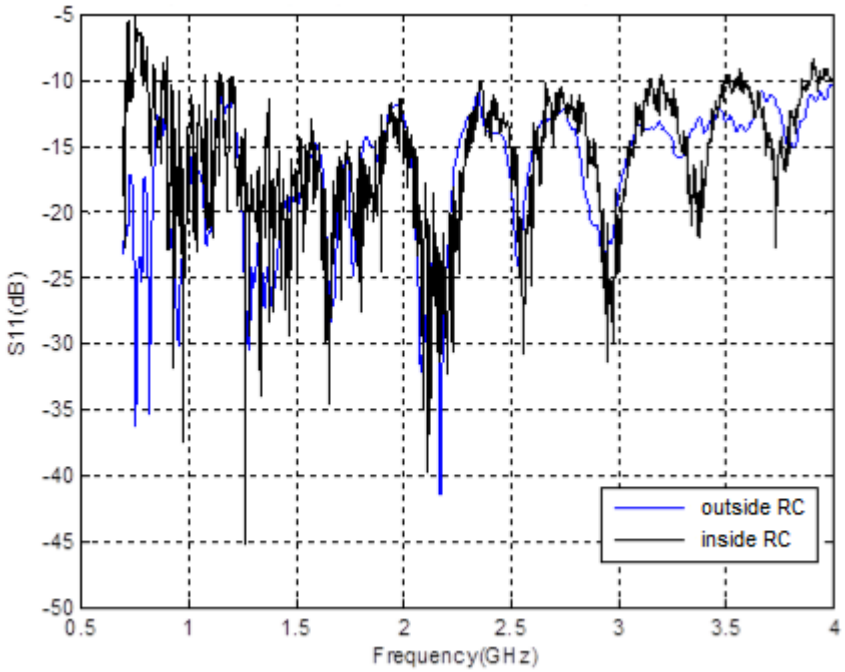


**Figure 6.11: Comparison of $S_{11}$ for the transmitting antenna outside and inside the RC**

As for Figure 6.10, Figure 6.11 shows that above 1.5 GHz, the $S_{11}$ of the antenna inside the RC is similar to that of the antenna in open space. As already stated, this technique requires that an average is done over many stirrer positions.

For frequencies lower than 1 GHz, the mismatch of the antenna has to be taken into account.

### 6.4 Correction factor

As mentioned previously, the antennas are not well matched to the cables at low frequencies. This mismatch is the cause of the discrepancy observed in Figure 6.10 and Figure 6.11. This can be compensated using a correction factor, as seen in the following lines.

The correction factor is introduced from Equation 3.26

$$K = \frac{1}{1-\left|S_{11}\right|^2}, \qquad \text{Equation 6.6}$$

and plotted in Figure 6.12.

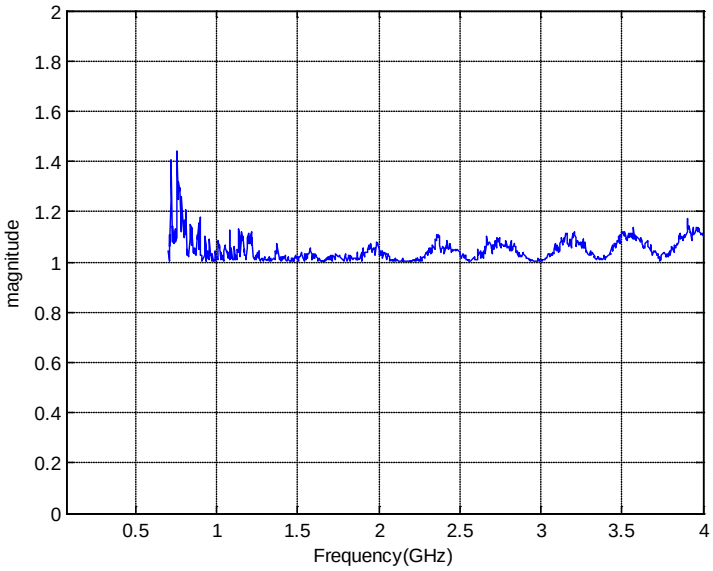


**Figure 6.12: Correction factor**

Figure 6.12 shows that the correction factor is close to 1 for frequencies higher than 1 GHz, and can be neglected in a first approach. However, it will be used to determine the chamber gain (Equation 3.26) in the next chapter.

### 6.5 Measurement precision with VNA

Measurements of $S_{11}$ and $S_{21}$ are carried out for 1601 frequency points (linear-spaced) between 800 MHz and 4 GHz at one stirrer position, and the sweep is repeated 101 times. A variation in the measured $S_{11}$ and $S_{21}$ values is noticed even when there is no stirrer rotation. An analysis has to be done to find its cause and to determine if this variability is within acceptable margins.

VNA measurement errors can be separated into systematic, random and drift errors. Correctable systematic errors are the repeatable errors that the system can measure. These errors are due to mismatch and leakage in the test setup, isolation between the reference and test signal paths and system frequency response. The system cannot measure and correct for the non-repeatable random and drift errors.

Figure 6.13 shows the measurement uncertainty of the transmission coefficient for the 8720ET VNA (8720ET datasheet, 1999), which is approximately 0.5 dB in the frequency range of 50 MHz to 8 GHz for expected values of $S_{21}$, except for the very small values (lower than -80 dB).

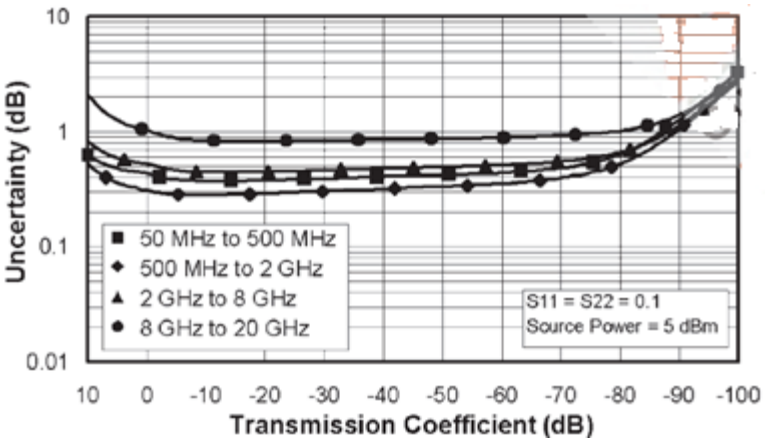


**Figure 6.13: Transmission measurement uncertainty (8720ET Transmission response Cal using 85052B calibration kit) (From 8720ET,1999)**

To verify this value of 0.5 dB found in the 8720ET datasheet, a first set of measurements is done at 1 GHz. This value is chosen because this frequency is within the frequency range of the RC and the antennas. For this set, the VNA sweeps with zero span and 101 measuring points; this is the same as using the VNA in CW mode. A sole acquisition is performed giving 101 measurements of the S-parameter at 1 GHz. Figure 6.14 presents the histogram of $|S_{11}|$ and $|S_{21}|$ measurements at 1 GHz.

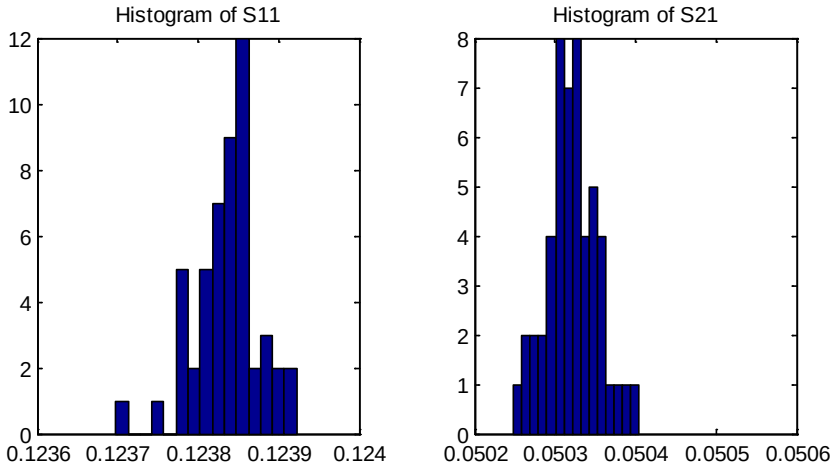


**Figure 6.14: Histogram of $|S_{11}|$ and $|S_{21}|$ at 1 GHz using VNA in CW mode**

The dispersion is here defined as $\Delta S = S_{Max} - S_{Min}$ where $S_{Max}$ and $S_{Min}$ are the maximum and minimum values, respectively. It is found that the relative dispersion of $|S_{11}|$ and $|S_{21}|$ is 0.1 % (0.02 dB) and 0.05 % (0.03 dB), respectively. The relative dispersion in dB is found from the ratio $S_{Max} / S_{Min}$.

For comparison purposes, a second analysis is done with the frequency sweep in a frequency range of 800 MHz to 4 GHz, with 1601 frequency points. From the set of swept frequencies, 1 GHz is chosen and the data histogram is given in Figure 6.15.

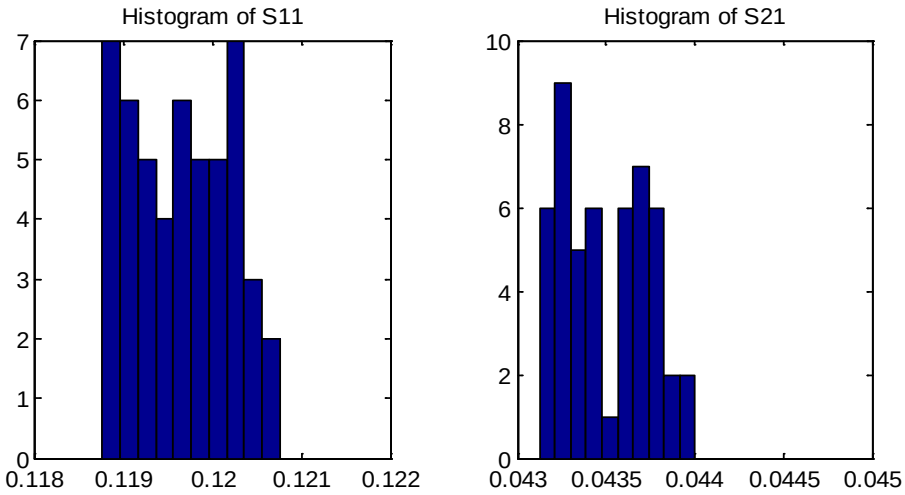


**Figure 6.15: Histogram of $|S_{11}|$and $|S_{21}|$at 1 GHz from the set of swept frequencies**

It is observed that the dispersion of $S_{11}$ is 1.6 % and $S_{21}$ is 2 %, which is 0.2 dB and 0.3 dB, respectively. Besides the fact that the dispersion in sweep mode is found larger than the one for CW mode, these measured values are in agreement with data given in Figure 6.13 which should be lower than 0.5 dB.

### 6.6 Summary

The RC attenuation was measured and found to range from -20 dB to -50 dB in the 800 MHz – 4 GHz frequency band. These large values are due to multiple causes: losses of the RC walls, leakage of the RC, and cables of low quality. To reduce the cable losses that impact on the $S_{21}$ determination, the calibration of the VNA has been done at the antenna level.

The $S_{11}$ of the antenna placed inside the RC and in free space were measured, and shown a similar pattern above 1.5 GHz although only one stirrer position was considered.

The dispersion of $S_{11}$ and $S_{21}$ was also measured as 0.2 dB and 0.3 dB, respectively, which is in agreement with the VNA datasheet.

The correction factor was determined: its non-unity values have to be taken into consideration.

# CHAPTER 7: MEASUREMENTS FOR THE STIRRER-EQUIPPED REVERBERATION CHAMBER

## 7.1 Test configuration

Real and imaginary values of $S_{21}$ are recorded in the frequency range of 800 MHz – 4 GHz for 200 stirrer positions. As the receiving antenna is of a Log-periodic planar type, that is an array of dipoles, $S_{21}$ is proportional to the $E_R$ component aligned with the dipoles, as illustrated in Figure 7.1.


**Figure 7.1: Log-periodic planar antenna (From Balanis, 2005)**

## 7.2 Stirring ratio

The aim of this procedure is to check that the RC is well-operated. This criterion was used by Ladbury (1999) prior to the introduction of the now standard uniformity test procedure. For each frequency and at all stirrer positions, the received power is derived from the measured $S_{21}$ using Equation 3.25. The maximum and mean values are then calculated. From Section 4.2.4, the stirring ratio is the ratio of the maximum power received by a wire antenna (over a full stirrer rotation) to the mean power received. For a perfectly matched antenna, the power received only depends on $|S_{21}|^2$. Figure 7.2 presents the stirring ratio of the CPUT reverberation chamber configured with one rotating stirrer.

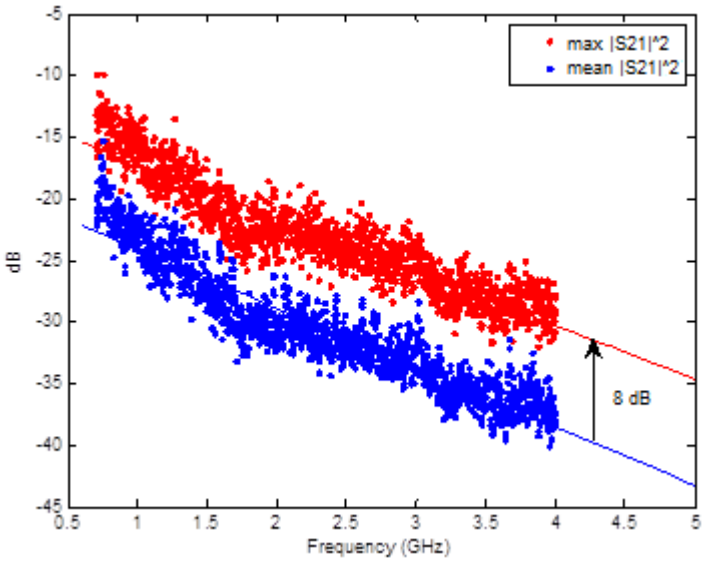


**Figure 7.2: Stirring ratio of the CPUT RC**

Firstly, it is seen that $|S_{21}|^2$ decreases with frequency, which is a property already shown in Equation 3.23. Secondly, there is a difference of approximately 8 dB between the maximum and mean values of $|S_{21}|^2$. Applying Equation 4.18 with $N = 200$, the theoretical stirring ratio is found to be 7.7 dB. This good agreement between theory and experimental data indicates that the RC is well-operated. Note that a similar stirring ratio is found using the correction factor given by Equation 6.6.

The following section focuses on the EM distributions inside the RC.

### 7.3 Distribution of EM quantities

The in-phase and quadrature components of $S_{21}$ are measured separately using the VNA. Figure 7.3 shows the scatter plot and the trace of the complex-valued $S_{21}$ as a function of paddle position at 800 MHz and 3.8 GHz.

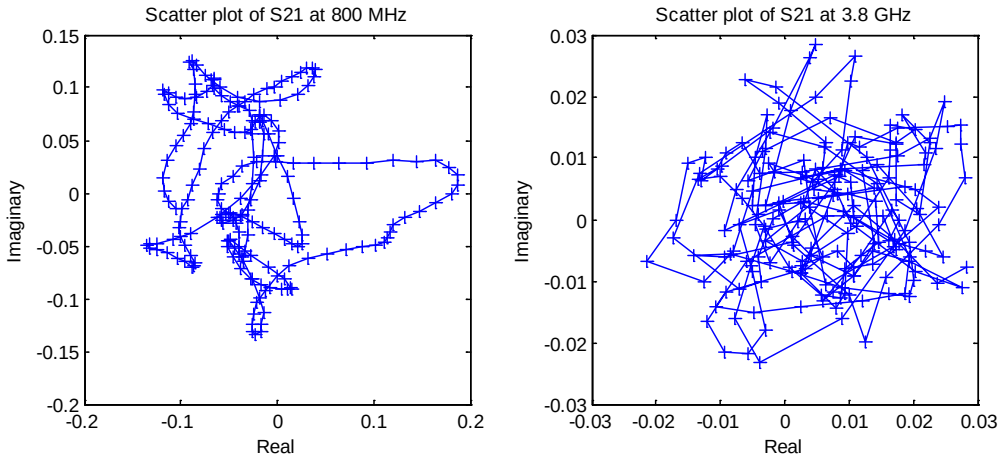


**Figure 7.3: Scatter plot of $S_{21}$ using one paddle with 200 stirrer positions**

At 800 MHz it can be seen that $S_{21}$ for consecutive stirrer positions are correlated; this property is investigated in Section 7.4.1. However, at 3.8 GHz the scatter plot reflects random behaviour.

#### 7.3.1 Gaussian distribution

A histogram of $S_{21}$ at 3.8 GHz for 200 stirrer positions is presented in Figure 7.4.

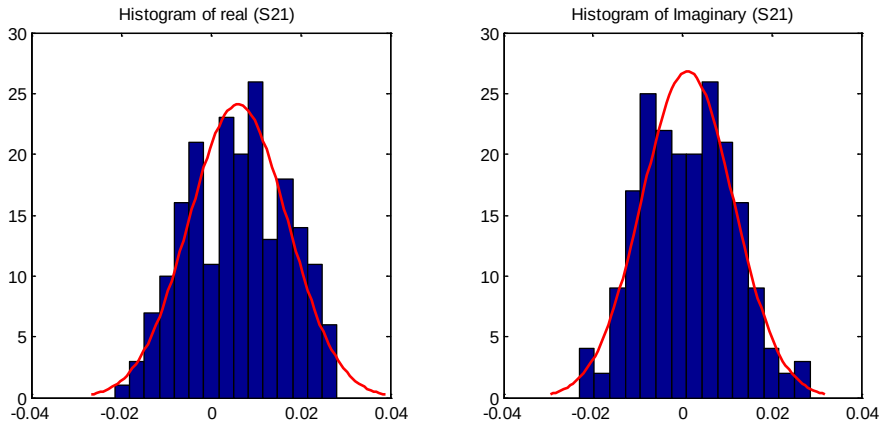


**Figure 7.4: Histogram of real and imaginary components of $S_{21}$ at 3.8 GHz**

These histograms indicate fairly good agreement with the Gaussian distribution (see Table 4.1). The average and the standard deviation of $S_{21}$ are computed and reported in Table 7.1.

**Table 7.1: Mean and standard deviation of $S_{21}$ for 200 stirrer positions at 3.8 GHz**

| $S_{21}$ | Mean | Standard Deviation |
|---|---|---|
| Real | 0.0061 | 0.0109 |
| Imaginary | 0.0012 | 0.0102 |

In Table 7.1 the standard deviations $\sigma$ can be considered as identical. Regarding the mean value, this quantity is close to zero for the imaginary part whereas it is slightly different from zero for the real part. This discrepancy may be attributed to a problem of estimation with only $N = 200$ measurements.

Finally, it is concluded that at 3.8 GHz, each component of $S_{21}$ has a zero-mean Gaussian distribution noted $\mathcal{N}(0, \sigma)$.

### 7.3.2 $E_R$ Rayleigh distribution

From Section 4.2.2, the magnitude of a rectangular component of the electric field is described by the Rayleigh distribution. The histogram of $E_R = |S_{21}|$ at 3.8 GHz for 200 stirrer positions is presented in Figure 7.5.

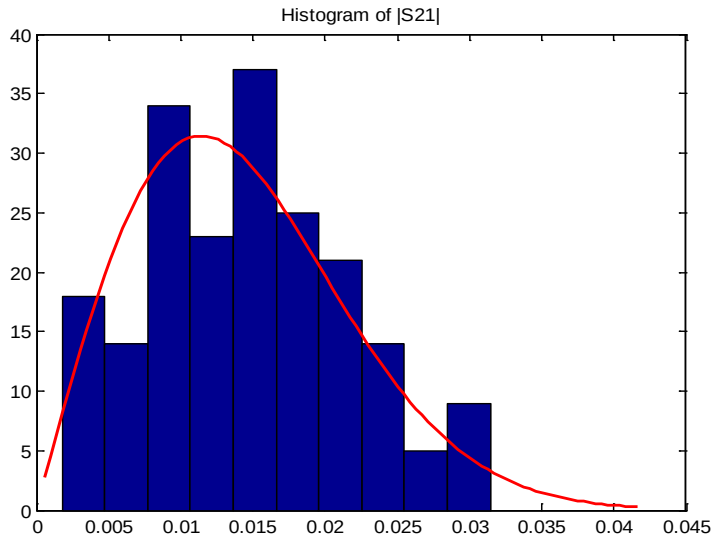


**Figure 7.5: Experimental and fitted values of $E_R = |S_{21}|$ at 3.8 GHz with 200 stirrer positions**

Visual inspection of this histogram indicates good agreement with a Rayleigh distribution (presented in solid red).

### 7.3.3 $E_R^2$ Exponential distribution

The power received by an antenna can be easily measured as it is proportional to $|S_{21}|^2$ This quantity represents $E_R^2$ that features an exponential distribution (see Table 4.1). This property of a well-operated RC is illustrated in Figure 7.6.

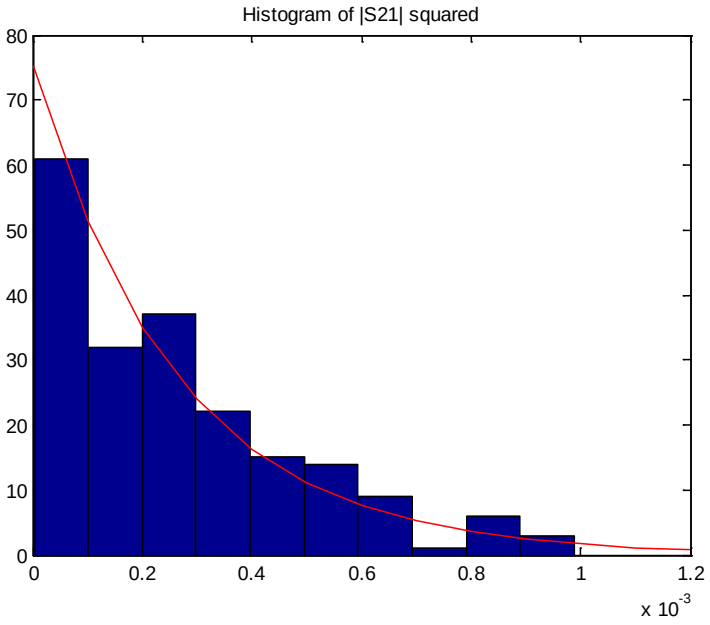


**Figure 7.6: Experimental and fitted values of $E_R^2 = |S_{21}|^2$ at 3.8 GHz with 200 stirrer positions**

Visual inspection of Figure 7.6 shows good agreement with the theoretical exponential distribution presented in Table 4.1.

### 7.4 Correlation between stirrer positions

In Section 7.3, theoretical PDFs have been compared to empirical ones derived from histograms. This technique to estimate empirical PDFs assumes that both data sets are identical and independent. Visual inspection of Figure 7.3 indicates that the 200 measured points are fairly uncorrelated at 3.8 GHz. Nevertheless, a quantitative method is now introduced to provide uncorrelated data. For this, the correlation coefficient between two stirrer positions $n$ and $n+k$ is computed for increasing values of $k$, called the lag. For instance, the correlation coefficient for lag = 2 is calculated from all $|S_{21}|$ values at position $n$ and $n+2$. This coefficient is plotted in Figure 7.7.

It has to be noted that the RC is equipped with two mechanical stirrers but only one stirrer is rotating. This procedure is valid for all subsequent measurements.

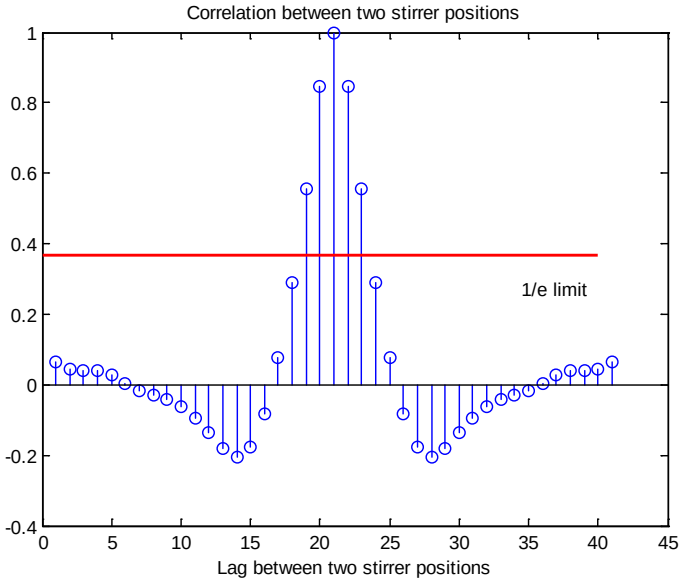


**Figure 7.7: Correlation of $|S_{21}|$ between two stirrer positions at 3.8 GHz**

Measured data used in Figure 7.7 shows that some correlation exists between two consecutive positions. As reliable statistics has to be done with uncorrelated data, a decimation has to be employed with at least $k = 3$. This means that only $N = 200/3 = 67$ stirrer positions must be considered. Figure 7.8 shows data decimated with $k = 3$.

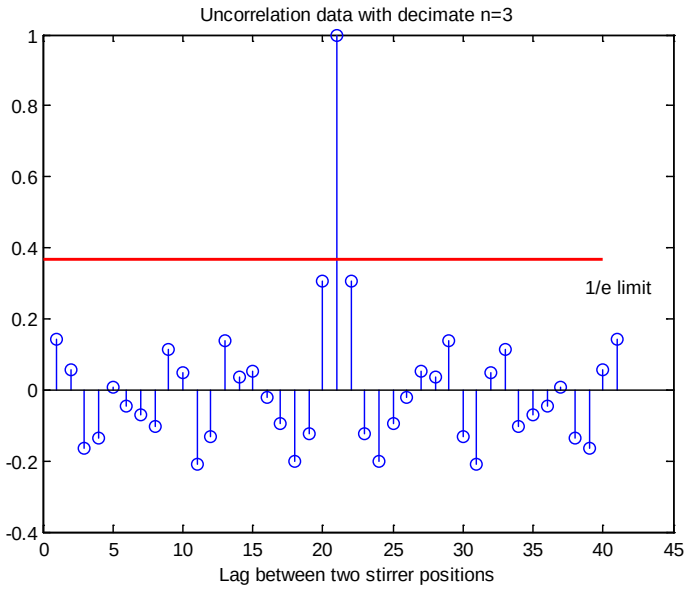


**Figure 7.8: Uncorrelated data with decimation *k* = 3**

The scatter plot shown in Figure 7.9 is the uncorrelated data obtained by decimating the data with $k = 3$ at 3.8 GHz.

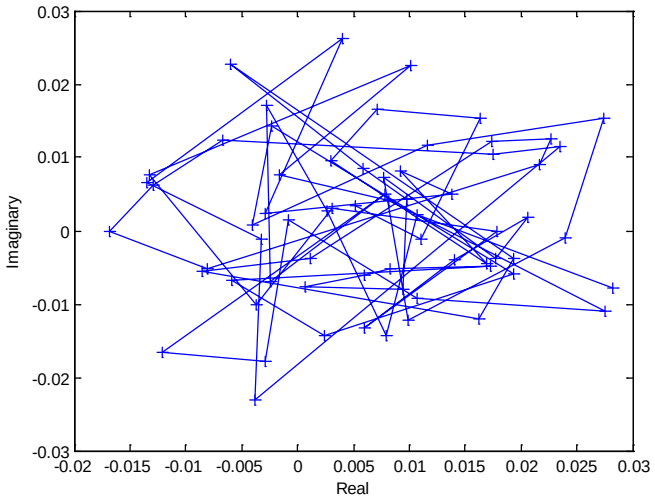


**Figure 7.9: Scatter plot of the data uncorrelated by decimation (*k* = 3), at 3.8 GHz**

The scatter plot reflects a fairly random behaviour, much better than the one observed in Figure 7.3. The number of stirrer positions at 3.8 GHz is reduced to 60 to obtain a better decorrelation.

This decimation technique is repeated for 800 MHz. The results are shown in Figure 7.10.

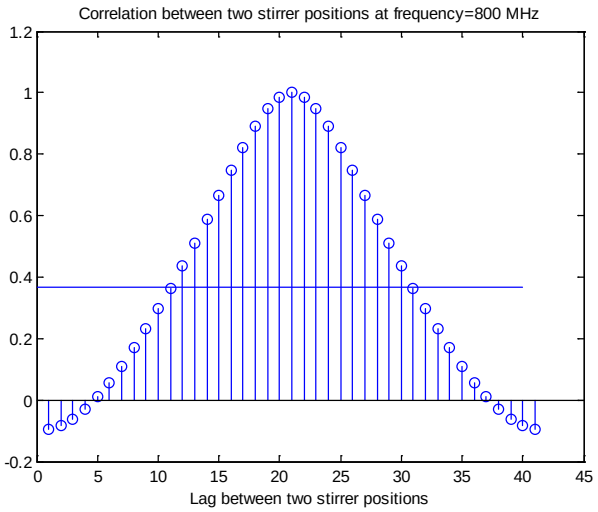


**Figure 7.10: Correlation coefficient of $|S_{21}|$ between two stirrer positions at 800 MHz**

Figure 7.10 shows that EM fields for close stirrer positions are strongly correlated, hence data needs to be decimated with at least $k = 10$. This means that at 800 MHz the number of stirrer positions should be $200/10 = 20$.

Finally, although taking 60 out of the 200 stirrer positions is suitable at high frequency, a different decimation must be done at low frequency to avoid correlation. The numbers of uncorrelated stirrer positions are reported in Table 7.2.

**Table 7.2: Number of uncorrelated stirrer positions**

| Frequency (GHz) | Decimation factor (*k*) | Number of uncorrelated stirrer positions (*N*) |
|---|---|---|
| 0.8 | 10 | 20 |
| 3.8 | 3 | 60 |

At 3.8 GHz, the value shown in Table 7.2 is comparable with the minimum value of $N = 50$ suggested in IEC 61000-4-21 standard, Table B.1. At 800 MHz, it would be advisable to increase the number of uncorrelated data: this can be done using frequency stirring.

### 7.5 Measured Q-factor

The Q-factor is related to the RC gain (Equation 3.43), which in turn depends on $S_{21}$ and $S_{11}$ as shown in Equations 3.24 and 3.25. This experimental value of the Q-factor is plotted in Figure 7.11.

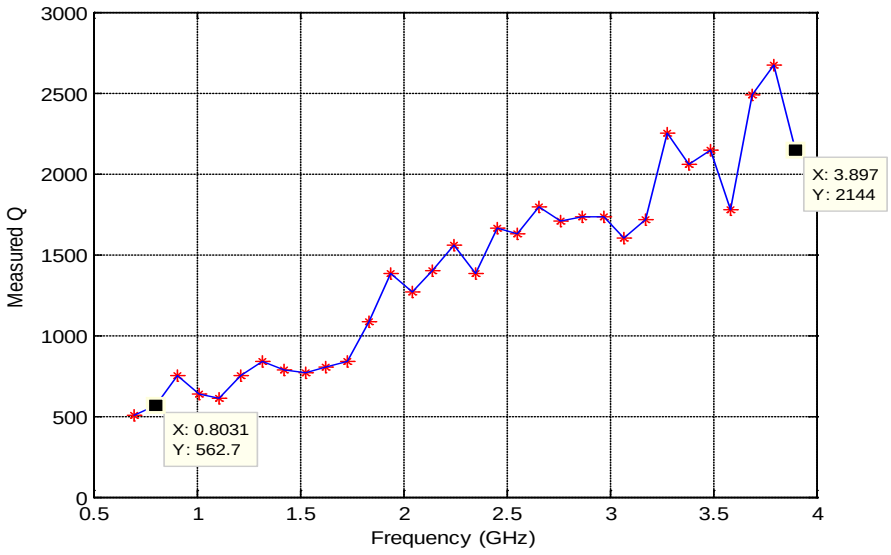


**Figure 7.11: Measured quality factor of the CPUT RC**

It is observed that the measured Q-factor at 800 MHz and 4 GHz is 563 and 2 144, respectively. These values are much lower than the theoretical ones presented in Figure 3.2 because losses from various origin (leakage material) are not modelled.

Finally, the experimental Q-factor is close to 2 000 at 3 GHz. It is recalled that the quality factor increases with the size of the RC (see Equation 3.40); for our rather small RC, this value is rather low, due to the imperfections of the original screen room. On another hand, a low Q factor means an important mixing of the mode and consequently a better uniformity.

## 7.6 Frequency stirring

There are two possibilities to increase the number of uncorrelated data measurements: either by using a second stirrer or to employ the frequency stirring technique. Frequency stirring is chosen and discussed below.

### 7.6.1 Correlation for frequency

Before using the frequency stirring technique, we need to verify that the data from two successive frequencies is uncorrelated. For the frequency span of 800 MHz – 4 GHz and taking 1601 points, the frequency spacing is $\Delta f_1 \cong \frac{4\times10^9 - 8\times10^8}{1601-1} \cong 2\,\text{MHz}$.

To verify that the measured data is uncorrelated, the correlation coefficient between measurements at two successive frequencies for increasing value of the lag (frequency spacing), and for all stirrer positions ($N = 200$), is computed. The variation of this coefficient with the lag is presented in Figure 7.12.

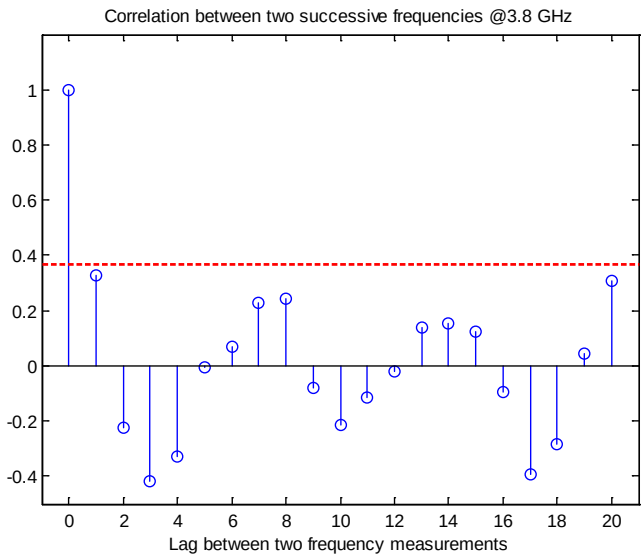


**Figure 7.12: Correlation coefficient between two frequencies around 3.8 GHz, with increasing lag, *N* = 200 stirrer positions**

In Figure 7.12, it is noted that even with a lag equal to one, data is uncorrelated for a 2 MHz frequency spacing. Therefore, frequency stirring is applicable with no need for decimation in frequency.

### 7.6.2 Interpretation of the frequency spacing

Section 7.6.1 shows that a 2 MHz frequency spacing yields statistical independence. Presented in this section is a verification of this value following a modal approach.

In the modal description of an RC, uncorrelation means that measurements for two successive frequencies belong to two different modes and these modes do not overlap. Each mode with resonant frequency $f_0$ is characterised by its quality factor $Q$ and the bandwidth associated with its frequency response is:

$$\Delta f_2 = \frac{f_0}{Q}. \qquad \text{Equation 7.1}$$

In order to have realistic values, $Q = 2\times10^3$ is read from Figure 7.11. Thus $\Delta f_2 = \frac{4\times10^9}{2\times10^3} = 2\,\text{MHz}$.

It is noticeable that $\Delta f_2 = \Delta f_1$, with $\Delta f_1$ the frequency spacing associated with the decorrelation. Moreover, the modal density can be derived from Equation 3.6:

$$\frac{dN}{df} \cong \frac{8\pi}{c}\cdot V \cdot \left(\frac{f}{c}\right)^2. \qquad \text{Equation 7.2}$$

This expression leads to an approximated 170 modes/MHz. This means that there are more than 300 mixing modes between two consecutive sampling frequencies.

### 7.6.3 Application of frequency stirring

To illustrate the frequency stirring technique, measurements for 60 independent stirrer positions and 11 successive frequencies close to 3.8 GHz are gathered. The histogram is shown in Figure 7.13.

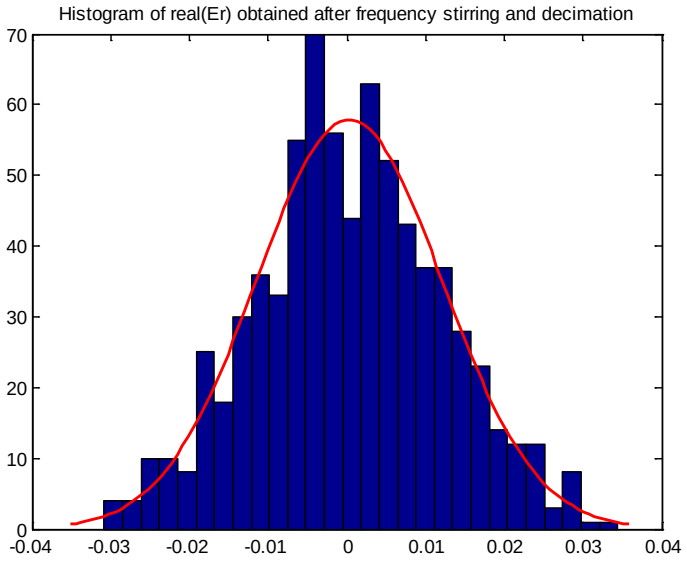


**Figure 7.13: Histogram of real $E_R$ obtained after frequency stirring and decimating at 3.8 MHz**

Compared to Figure 7.4, it is noticed that with a large sample ($660 = 60 \times 11$) of uncorrelated data, the empirical PDF of $E_R$ is close to a Gaussian distribution. Furthermore, it is noticeable that the mean value is closer to zero. Table 7.3 shows the mean value and the standard deviation of $S_{21}$ from 660 uncorrelated data points.

**Table 7.3: Mean and standard deviation of $S_{21}$ from 660 uncorrelated data points**

| $S_{21}$ | Mean | Standard Deviation |
|---|---|---|
| Real | 0.0003 | 0.0118 |
| Imaginary | 0.0044 | 0.0120 |

The standard deviations $\sigma$ can be considered as identical, and the mean value close to zero. Finally, it is concluded that each component of $S_{21}$ has a zero-mean Gaussian distribution $\mathcal{N}(0, \sigma)$.

It is seen that frequency stirring allows a better estimation of statistical parameters. The following section gives another application of frequency stirring.

### 7.7 Uniformity test

In addition to the two methods previously used to assess the behaviour of the RC (stirring ratio, and analysis of empirical PDFs of the fields), the uniformity test described in IEC 61000-4-21 is the standard way to calibrate an RC. The purpose of this test is to verify that the EM fields have statistically the same magnitude, within a defined uncertainty interval, for all polarisations and for all directions of arrival at all locations within the working volume, for a given number of stirrer positions.

As seen in Figure 2.9, EM fields within the chamber are considered as uniform if their standard deviation is within 3 dB above 400 MHz, and 4 dB at 100 MHz decreasing linearly to 3 dB at 400 MHz, and within 4 dB below 100 MHz.

To compute the quantity $\sigma_{\mathrm{dB}}$ defined in Equation 2.2, measurements must provide $E_R$. As a 3-D probe was not available, the short dipole antenna shown in Figure 7.14 was used.

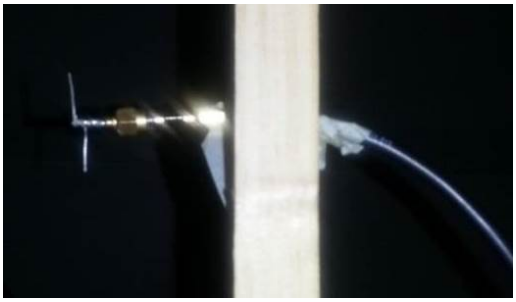

**Figure 7.14: Short dipole antenna used instead of E-field probe**

According to IEC 62000-4-21 standard, $\sigma$ should be determined from measurements at a minimum of 8 points (in order to obtain $8 \times 3 = 24$ samples). In this work, data is collected at 12 points distributed on the limits of the working volume shown in Figure 7.15.

**Figure 7.15: RC working volume**

The antenna presented in Figure 7.14 is used to measure $E_R$ at 12 sufficiently different locations. For each of these points, 2 individual axes (*x*, *y*) are measured, the third one being discarded for practical reasons: uncorrelation to the other measurements would only be obtained for a cumbersome orientation of the dipole. Thus 24 values of $E_R$ are measured per frequency.

The field uniformity is determined by first finding the maximum value $E_{R\,\max}$ and the mean value of the maximum $\left\langle E_{R\,\max} \right\rangle$ for 60 stirrer positions. These values are checked to be uncorrelated. Equation 2.2 is used to derive the normalised standard deviation $\sigma_{\mathrm{dB}}$ expressed in dB.

The frequency stirring technique is then employed to increase the accuracy of the $\sigma_{\mathrm{dB}}$ estimation. Eleven nearby frequencies are considered (hence, a span of 10 $\times$ 2 = 20 MHz), and $\sigma_{\mathrm{dB}}$ is estimated from $11 \times 24 = 264$ maximum values.

Figure 7.16 shows the variation of $\sigma_{\mathrm{dB}}$ with frequency.

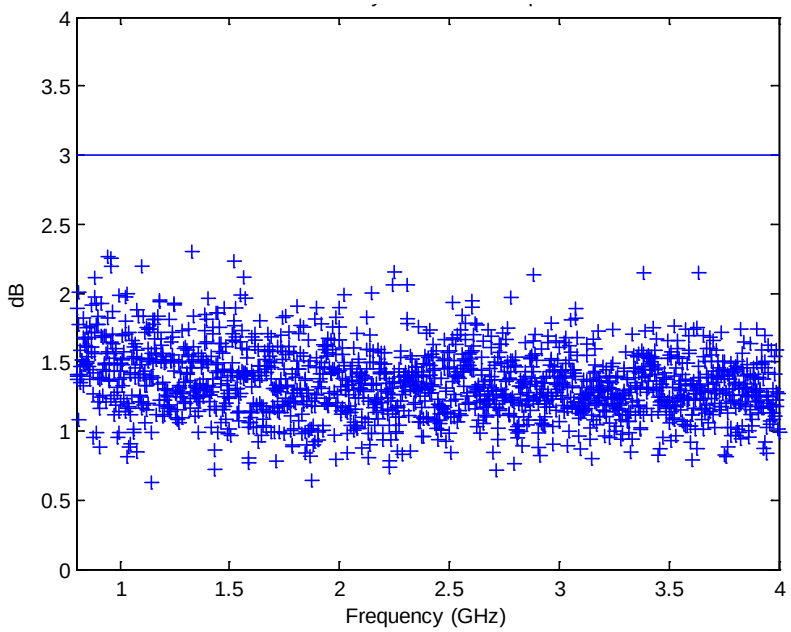


**Figure 7.16: Field uniformity estimator $\sigma_{\mathrm{dB}}$ obtained at 12 positions, for two polarisations, and using frequency stirring**

Figure 7.16 show that $\sigma_{\mathrm{dB}}$ is approximately 1.5 dB.

Recalling that $\sigma_{\mathrm{dB}}$ is used to assess the field uniformity and that it must fall within 3 dB for a well-operated RC (Figure 2.9), it is concluded that the constructed RC is well-operated in the frequency range of 800 MHz to 4 GHz.

# CHAPTER 8: CONCLUSIONS AND RECOMMENDATIONS

An electromagnetically screened room was successfully converted into a Reverberation Chamber equipped with two mechanical stirrers. Stirrers were designed and manufactured, and a fully automated environment (stirrer rotation and measurement) was created. In the delineation of this work, only the vertical stirrer will be rotated. The frequency range of interest for measurements in the CPUT RC was initially defined between 300 MHz and 4 GHz, because the lowest usable frequency for the RC is about 300 MHz. However, due to the availability of antennas with a frequency range of 800 MHz – 4 GHz, measurements were done in this range throughout the study. This frequency range is suitable to test CubeSat subsystems in the L- and S-bands.

## 8.1 Main findings

The theoretical background of an RC was recalled in depth, for both the deterministic model of a cavity and the statistical approach for a reverberating environment. Furthermore, advanced techniques used for order statistics were applied to express the maximum PDFs for Rayleigh and Exponential parent distributions.

First, the empty cavity was analysed through simulation. The first five modes of the empty cavity were simulated and were compared to the theoretical calculations. The agreement in results enables a possible numerical study of the RC (cavity equipped with stirrer) for low frequencies.

An automated measurement setup was implemented. Special attention was given to important issues, such as measurements accuracy, compensation of cable losses, and antenna mismatch using a correction factor.

Mechanical stirrers were designed and the electromechanical components (stepper motor, stepper driver, and controller) carefully selected. The electromechanical system and VNA are controlled by a computer program to enable fully automated measurements.

The RC performance was first studied using the stirring ratio. The experimental value agreed with the theory, indicating that the RC was well-operated in the frequency range of 800 MHz – 4 GHz. This was also borne out by the measured field uniformity estimator $\sigma_{\mathrm{dB}} \cong 1.5\,\mathrm{dB}$ over this frequency range.

Empirical distributions of EM quantities ($E_R$ and $E_R^2$) were also determined and agreed with the theoretical ones (Rayleigh and Exponential distributions, respectively).

## 8.2 Response to the research questions

The existing screened room at CPUT was successfully converted into an RC by installing two mechanical stirrers, mounted vertically and horizontally. Mechanical stirrers were designed for a LUF of $f = 300$ MHz, according to the IEC 61000-4-21 standard.

To achieve automated measurements in the RC, a mechanical stirrer was connected to the stepper motor, which is controlled by a stepper driver. The stepper motor was selected based on the calculated holding torque. An Arduino Uno board was used to control the stepper driver, and the VNA was interfaced with a computer through MATLAB®.

The experimental quality factor of the RC was found to be close to 2 000 at 3 GHz. This rather low value yields an important mixing between nearby modes and should lead to a satisfactory uniformity at low frequency. The drawback is that more power is needed for a given strength of the electric field.

Statistical independence of data for stirrer positions and for frequency was also addressed. Using a decimation technique, 60 uncorrelated stirrer positions were used to perform reliable statistical analyses at 3.8 GHz, and 20 positions for measurements at 800 MHz.

Eleven uncorrelated successive frequencies were considered for frequency stirring. This technique was used to estimate the field uniformity according to IEC 61000-4-21 standard. It was concluded that the reverberation chamber passed the validation procedure by demonstrating its ability to generate the required field uniformity within the accepted uncertainty level.

## 8.3 Recommendations

- We recommend the use of antennas in frequency range of 300 MHz – 1 GHz to experimentally determine the LUF.
- Further research and measurements can be conducted with a 3-D probe instead of a short dipole used in this research. This study should include an analysis of the field strength uniformity over space and frequency, for a specific E-field value, e.g. 3V/m.
- Further measurements should be made to study the improvement in the correlation when the second stirrer is rotating.
- Simulations should be done not only for the first modes, but also at a higher frequency, for example, closer to the LUF.
- Modelling can be done with another electromagnetic solver, *e.g.*, FEKO® software in order to compare its performance with CST Microwave Studio®.
- Susceptibility tests should be conducted and applied to actual CubeSat hardware.

## REFERENCES


Andersson, M., Wolfgang, A., Orlenius, C., & Carlsson, J. 2009. Measuring Performance of 3GPP LTE Terminals and Small Base Stations in Reverberation Chambers. *Long Term Evolution: 3GPP LTE Radio and Cellular Technology*, 413.

Arnaut, L. R., 2001. Operation of electromagnetic reverberation chambers with wave diffractors at relatively low frequencies. *IEEE Transactions on Electromagnetic Compatibility*, 43: 637-653.

Arnaut, L. R., 2003. Statistics of the Quality factor of a rectangular reverberation chamber. *IEEE Transactions on Electromagnetic Compatibility*, 45: 61-76.

Bäckström, M., Lundén, O., & Kildal, P. S. 2002. Reverberation chambers for EMC susceptibility and emission analyses. *Review of Radio Science 1999-2002*: 429-452.

Balanis, C. A. 2005. *Antenna theory: analysis and design*. John Wiley & Sons.

Besnier, P., & Démoulin, B. 2013. *Electromagnetic reverberation chambers*. John Wiley & Sons.

Besnier, P., Lemoine, C., & Sol, J. 2015. Various estimations of composite Q-factor with antennas in a reverberation chamber*. In Electromagnetic Compatibility (EMC), 2015 IEEE International Symposium,* 1223-1227

Bruns, C. 2005. *Three-dimensional simulation and experimental verification of a reverberation chamber* (Doctoral dissertation, Swiss Federal Institute of Technology Zurich).

Carlberg, U., Kildal, P.S. & Carlsson, J., 2005. Study of antennas in reverberation chamber using method of moments with cavity Green's function calculated by Ewald summation. *IEEE transactions on electromagnetic compatibility*, 47(4):805-814.

Cerri, G., Primiani, V. M., Monteverde, C., & Russo, P. 2009. A theoretical feasibility study of a source stirring reverberation chamber. *IEEE Transactions on Electromagnetic Compatibility*, *51*(1): 3-11.

CISPR/A & IEC SC 77B. 2003. *IEC 61000-4-21 – Electromagnetic Compatibility (EMC) – Part 4-21: Testing and measurement techniques – Reverberation chamber test methods.* International Electronical Commission (IEC) International standard.

Clark, T. L., McCollum, M. B., Trout, D. H., & Javor, K. 1995. *Marshall Space Flight Center Electromagnetic Compatibility Design and Interference Control (MEDIC) Handbook*. NASA, Reference Publication, 1368.

Coates, A., & Duffy, A. 2007. Maximum working volume and minimum working frequency tradeoff in a reverberation chamber. *IEEE Transactions on Electromagnetic Compatibility*, 49(3):719-722.

Cottard, G., & Arien, Y. 2006. Anechoic chamber measurement improvement. *Microwave Journal*, *49*(3):94.

Corona, P., Ladbury, J., & Latmiral, G. 2002. Reverberation-chamber research-then and now: a review of early work and comparison with current understanding. *IEEE Transactions on Electromagnetic Compatibility*, *44*(1): 87-94.

Crawford, M. L., & Koepke, G. H. 1986*. Design, Evaluation, and use of a Reverberation Chamber for Performing Electromagnetic Susceptibility/Vulnerability Measurements, NBS Tech*. Note 1092. Washington: US government printing office.

Davenport, W. B., & Root, W. L. 1958. *An introduction to the theory of random signals and noise* (159). New York: McGraw-Hill.

Dunn, J.M. 1990. Local high frequency analysis of the fields in a mode-stirred chamber, *IEEE Transactions on Electromagnetic Compatibility,* EMC-32:53-58.

Dunlap, C.R., 2013. *Reverberation chamber characterisation using enhanced backscatter coeffient measurement*. Doctoral dissertation, University of Colorado.

Eser, S., & Sevgi, L. 2010. Open-area test site (OATS) calibration. *Antennas and Propagation* Magazine, IEEE, 52(3): 204-212.

Ferrara, G., Migliaccio, M., & Sorrentino, A. 2007. Characterization of GSM non-line-of-sight propagation channels generated in a reverberating chamber by using bit error rates. *IEEE Transactions on Electromagnetic Compatibility*, *49*(3): 467-473.

Genender, E., Holloway, C. L., Remley, K. A., Ladbury, J. M., Koepke, G & Garbe, H. 2010. Simulating the multipath channel with a reverberation chamber: Application to bit error rate measurement. *IEEE Transactions on Electromagnetic Compatibility*, 52(4): 766-777.

Goldsmith, K. 1999. Reverberation Chambers–What Are They?. *IEEE EMC Society Newsletter*.

Grant, M. 2005. Quick Start for Beginners to Drive a Stepper Motor. *Freescale Semiconductors*. [13 July 2013]

Hill, D. A. 1994. Electronic mode stirring for reverberation chambers. *IEEE Transactions on Electromagnetic Compatibility*, *36*(4): 294-299.

Hill, D. A. 1996. A reflection coefficient derivation for the Q of a reverberation chamber. *IEEE Transactions on Electromagnetic Compatibility*, *38*(4): 591-592.

Hill, D. A. 1998. Plane wave integral representation for fields in reverberation chambers. *IEEE Transactions on Electromagnetic Compatibility,* 40(3):209-217.

Holloway, C. L., Hill, D. A., Ladbury, J. M., Wilson, P. F., Koepke, G., & Coder, J. 2006. On the use of reverberation chambers to simulate a Rician radio environment for the testing of wireless devices. *IEEE Transactions on Antennas and Propagation*, *54*(11): 3167-3177.

Hughes, A. 2005. *Electric Motors and Drives: Fundamentals, Types and Applications*. Newnes.

Inteference technology. 2009. *Reverberation Chamber for EMC testing*. http://www.interferencetechnology.com/reverberation-chamber-for-emc-testing/ [10 June 2013].

Krauthäuser, H.G., Nitsch, J. n.d. Effects of the variation of the excitation and boundary conditions of mode-stirred chambers and consequences for calibration and measurements. *Otto-von-Guericke-University Magdeburg, Germany*, 1-6 [25 July 2014].

Kildal, P. S., Carlsson, C., & Yang, J. 2002. Measurement of free-space impedances of small antennas in reverberation chambers. *Microwave and Optical Technology Letters*, *32*(2), 112-115.

Kuphaldt, T. R. 2006. Lessons in electric circuits, Volume I-DC. 5th ed. Open book project.

Ladbury, J., Koepke, G., & Camel, D. 1999. *Evaluation of the NASA Langley Research Center mode-stirred chamber facility, NIST technical note 1508*. Washington: US government printing office.

Leferink, F., Boudenot, J. C., & van Etten, W. 2000. Experimental results obtained in the vibrating intrinsic reverberation chamber. *IEEE International Symposium on Electromagnetic Compatibility,* (2):639-644.

Lehman, T. H., & Freyer, G. J. 1997. Characteriation of the maximum test level in a reverberation chamber. In *Electromagnetic Compatibility, IEEE 1997 International Symposium on Electromagnetic Compatibility*, 44-47.

Lemoine, C., Amador, E., & Besnier, P. 2011. On the K-factor estimation for Rician channel simulated in reverberation chamber. *IEEE Transactions on Antennas and Propagation*, *59*(3): 1003-1012.

Liu, B.H, Chang, D.C. & Ma, M.T. 1983. *NBS Technical Notes 1066: Eigen modes and the composite quality factor of a reverberation chamber.* Washington: US government printing office.

Malaric K. 2001. *Electromagnetic Compatibility Analysis using TEM cells.* http://www.eetimes.com/document.asp?doc_id=1255099 [16 July 2016]

Maral, G., & Bousquet, M. 1993. Satellite communications systems. Systems, techniques and technology. *Wiley Series in Communication and Distributed Systems.* 2nd ed. New York: Wiley.

Montrose, M. 1994. Fundamentals Of EMC. In *SCV EMC'94, IEEE*: 1b1-1b9.

Moore, G. 2003. Development, implementation and management of a system level EMC design mitigation plan. In *Electromagnetic Compatibility, 2003 IEEE International Symposium on Electromagnetic Compatibility,* 1:173-176.

Mosig, J. R., & Gardiol, F. E. 1983. Analytical and numerical techniques in the Green's function treatment of microstrip antennas and scatterers. In *IEE Proceedings H :Microwaves, Optics and Antennas,* 130(2):175-182. IET Digital Library.

Musso, L. 2003. Assessment of reverberation chamber testing for automotive applications. *PbII Thesis,* Politecnico di Torino, Turin, Italy, UniversitC de Lille.

Nattaphong, B. 2008. *A TEM cell design to study Electromagnetic radiation exposure form cellular phones.* University of Missouri.

Orjubin, G. Richalot, E. Picon, O. & Legrand, O. 2009. ScienceDirect: New approaches in Electromagnetic Compatibility: *Wave chaos techniques to analyze a modeled reverberation* chamber. Comptes Rendus Physique, 10:42-53. March 2009.

Orjubin, G., Richalot, E., Picon, O., & Legrand, O. 2009. Wave chaos techniques to analyze a modeled reverberation chamber. *Comptes Rendus Physique*, *10*(1):42-53.

Panetta, P. V., Culver, H., Gagosian, J., Johnson, M., Kellogg, J., Mangus, D., Michalek, T., Sank, V. & Tompkins, S. 1998. NASA-GSFC CubeSat technology development. *Proceedings of the 12th Annual AIAA/Utah State University Conference on Small Satellites.*

Papoulis, A., & Pillai, S. U. 2002. *Probability, random variables, and stochastic processes*. Tata McGraw-Hill Education.

Pfenning, S., & Krauthauser, H.G. 2013. Comparison of methods for determining the number of independent stirrer positions in reverberation chambers. *International Symposium on Electromagnetic Compatibility (EMC EUROPE 2013)*, 2-6 September 2013:431-436.

Pozar, D. M. 2005. *Microwave engineering*. 3rd ed., MA John Wiley & Sons.

Rajamani, V., Bunting, C., & Freyer, G. 2009. Why consider EMC testing in a reverberation chamber. *10th International Conference on Electromagnetic Interference & Compatibility, 2008.* INCEMIC 2008. Bangalore, 26-27 November 2008:303-308.

Roman, M., & Van Zyl, R. 2011. Passive field uniformity enhancement in reverberation chambers*. In AFRICON, 2011*, September 2013:1-6.

Satav, S. M., & Agarwal, V. 2008. Do-it-yourself fabrication of an open TEM Cell for EMC pre-compliance. *IEEE EMC Society Newsletter*, 218:66-71.

Scott, L. 1998. Mode-stir measurement techniques for EMC theory and operation.

Thye, H., Armbrecht. G., & Koch M. 2009. Pulsr propagation in gigahertz transverse electromagnetic cells. *IEEE Transactions on Electromagnetic Compatibility,* 51(3):592-603.

Visser, D.F. 2009. ZACUBE-1 (1U CubeSat) Mission Requirements and Technical Specifications. Bellville: Cape Peninsula University of Technology. [Unpublished Technical Report].

Wang, Y. J., Koh, W. J., Tai, Y. K., Lee, C. K., & See, K. Y. 2002. Evaluating field uniformity of a mini-reverberation chamber with two mechanical stirrers. In *Electromagnetic Compatibility, 2002. EMC 2002. IEEE International Symposium on Compatibility,* 2:795-798.

Warin, D. 1996. Exploitation de l'environnement electromagnetique genere dans une chambre reverberante a brasseur de modes pour l'evaluation du seuil de dysfonctionnement de circuits integers (Doctoral dissertation).

Wantai. 2000. *Manual of 2-phase hybrid stepper motor driver DQ542MA Q542MA micro-stepping driver* [15 February 2014].

Weeks, F. 2000. *Stress analysis of a tuner for an electromagnetic reverberation chamber (No. DSTO-TN-0272)*. Defence Science and Technology Organisation Melbourne: Australia.

Wertz, J. R., & Larson, W. J. 1999. *Space mission analysis and design.* 3rd ed. California: Microcosm.

Wiles, M., & Rodriguez, V. 2010. Choosing the right chamber for your test requirements. *EMC Directory & Design Guide*.

Zhao, Y., Wei, G., Cui, Y., Fan, L., Pan, X., & Wan, H. 2015. Acceleration technique of modelling lossy reverberation chamber using FDTD method based on quality factor. IEEE Antennas and Wireless Propagation Letters, 14:686-689.

# APPENDICES

## Appendix A: Half and micro-stepping

Presented below are the different modes of operation of a stepper motor.

### Half-step mode

In half-step mode, one winding is energised first and then two windings are energised alternately, which results in the rotor rotating half the distance (Grant, 2005).Shown in Figure A.1 is the motor rotation sequence for half-step.

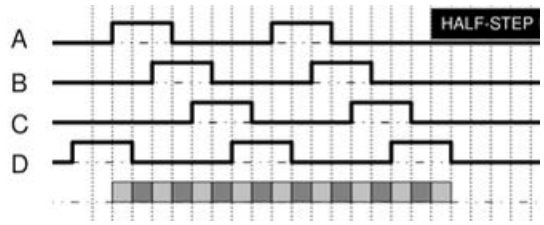


**Figure A.1: Motor rotation sequence for half-step**

A, B, C and D represent the stepper motor coil.

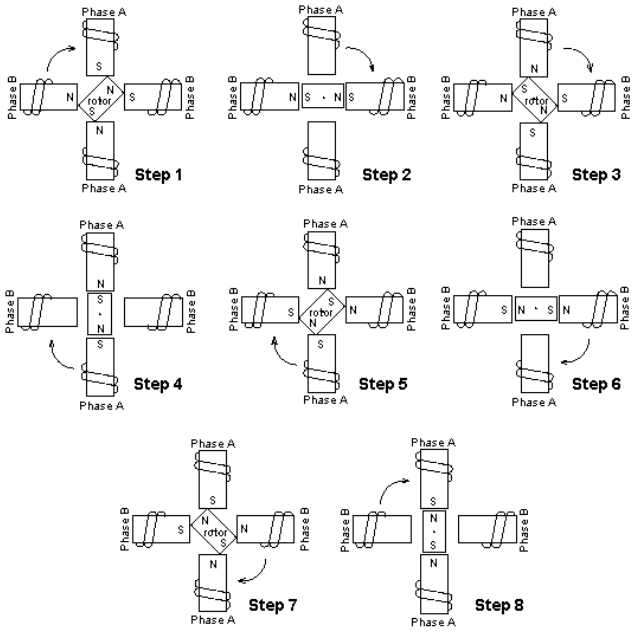


**Figure A.2: 8 steps motor rotation illustrating half-steps**

### Micro-stepping

Micro-stepping mode controls the current in the motor winding to a degree that further subdivides the number of positions between poles, hence, dividing a full step into smaller steps. This is to reduce the current that flows through the winding to a fraction of either the full-on current in one direction or the full-on current in the opposite direction.

The goal of micro-stepping is to create a motor that runs as smoothly as possible by allowing the motor to be pushed or pulled in increments rather than with full force. At the same time, it allows the rotor to stop in between the positions allocated for full steps (Grant, 2005). Figure A.3 illustrates currents in the stator during micro-stepping and the resultant current.

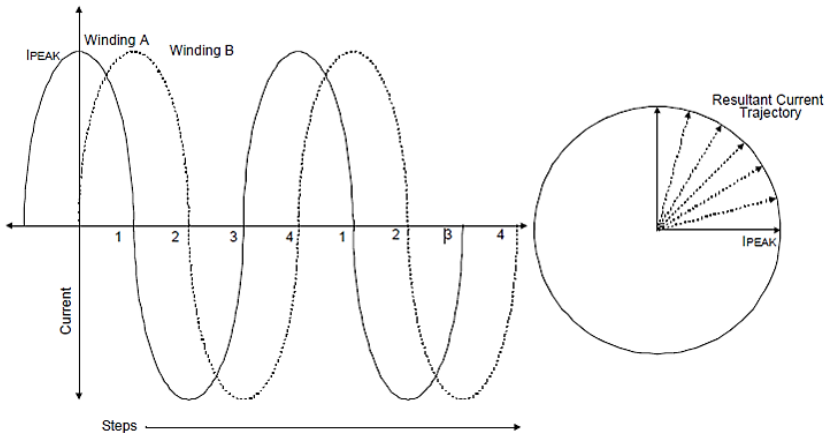


**Figure A.3: Currents in stator during micro-step and resultant current (From RS 535-0445 stepper motor)**

Current is varied in one winding with a sine function of an angle and in the other winding with a cosine function of angle. When the windings are energised, each of the windings produces a flux in the air gap that is proportional to the current in that winding. The flux in the air gap is directly proportional to the vector sum of the winding currents, in the resultant vector direction.

## Appendix B: PWM mode of the stepper driver

Following the specifications, the driver is supplied with 20 V and the stepper motor must be driven with a voltage rating of 3.2 V. To achieve this matching, the driver is operated in PWM mode, as illustrated hereafter.

Figure B.1 represents the voltages measured at each coil of the selected stepper motor, for full step mode. The blue wave is measured at point A and magenta is measured at point B. The green wave represents the voltage $V = V_A - V_B$ across the coil.

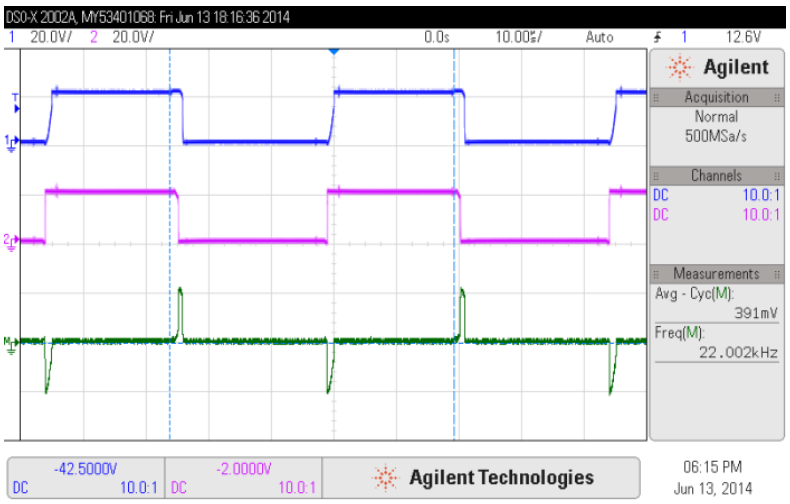


**Figure B.1: Measured waveform for voltage of different values of duty cycle at point A and B**

It can be seen that the waveforms are consistent with the PWM mode, with a chopping frequency close to 22 kHz. The voltage applied to the coil is rectangular signal, which mean value is lower than 3 V.

## Appendix C: Software implementation

This section focuses on how the automated measurement is achieved.

### Communication between Arduino Uno board and MATLAB®

The following are guidelines that are necessary to successfully establish communication between MATLAB® and the Arduino Uno board.

Communication between the Arduino Uno board and MATLAB® has to be checked first with the installation file called "install_arduino.m". This installation file should be executed in MATLAB® and one has to verify that "AF Motor.h" file is in the library. There is an arduino.exe and "srv.pde", which is found in "ArduinoIO\pde\srv". The srv.pde should be uploaded and if the verification works but cannot be uploaded, Arduino's drivers need to be verified. Arduino is connected to MATLAB® with a command aa = arduino('COM??'). This should be first checked to establish which COM port is used by the Arduino under the Arduino software (Tools/Serial Port). The USB port should be changed if COM1 is found because COM1 cannot be used to exchange data. These steps should only be done once.

### MATLAB® script for automated data acquisition

```
% Naftali Verena
% VNA communications using Form5
% The VNA must be warm up one heure before it run.
% The VNA must be switched on before running matlab
% Last edited: 01/08/14

%We take measurements of S11 and S21 for N stirrer position.
%sweep=1601 points at the frequency range 800MHz-4GHz
%Calibration has been done for this frequency range compatible with
%logperiodic antenna


%% Initialisation of Arduino
%Removal of the COM3 Port if it is already used
delete(instrfind({'Port'},{'COM3'}))
delete(instrfind({'Port'},{'COM4'}))

% New folder way for data saving
cd('C:\Users\211170836\Desktop\Arduino installation Pack\Verena\data');

% Connection to Arduino and the VNA
aa = arduino('COM3');
bb = arduino('COM4');

% initialize the digital pin as an output
aa.pinMode(10,'output'); % pin 10 as PULSE
aa.pinMode(9,'output'); %  pin 8 as ENABLE
aa.pinMode(8,'output'); %  pin 9 as DIRECTION

% initialize DIRECTION and ENABLE
aa.digitalWrite(9,1); %  set ENABLE to HIGH (0)
aa.digitalWrite(8,0); %  set DIRECTION to HIGH (1)
pause(0.5);
```

```
% initialize the digital pin as an output
bb.pinMode(10,'output'); % pin 10 as PULSE
bb.pinMode(9,'output'); %  pin 8 as ENABLE
bb.pinMode(8,'output'); %  pin 9 as DIRECTION

% initialize DIRECTION and ENABLE
bb.digitalWrite(9,1); %  set ENABLE to HIGH (0)
bb.digitalWrite(8,0); %  set DIRECTION to HIGH (1)
pause(0.5);

%% INITIALISATION OF VNA
%
% Adressing of the VNA
visa_addr='GPIB0::16::INSTR';
% VNA is represented by obj1
VNA = visa('agilent', visa_addr);

% Max out buffer size for largest possible read of 1601 points in FORM5
set(VNA,'InputBufferSize', 13000);

%                                   SETTINGS OF VNA
       %
fopen(VNA);
fprintf(VNA, 'POIN 1601'); % Nb of frequency points
% We use the highest number of points to further employ Frequency Stirring
% Technique.
fprintf(VNA, 'STAR 700e6'); % start frequency
fprintf(VNA, 'STOP 4e9'); % stop frequency
fprintf(VNA, 'CORR  ON'); %Lock the calibration
fprintf(VNA, 'MARKDISC  0'); %Lock the marquer
fclose(VNA);

%-------------------------------------------------------------
%% BEGINNING OF THE LOOP TO TAKE MEASURES                              %


currentstep_aa = 0;
N_step = 20;
flag = 1;
frame_duration=256/N_step;

for currentstep_bb= flag:N_step;
    bb.servoAttach(1);
    pause(frame_duration)
    bb.servoDetach(1);
    pause(4)
    currentstep_bb
while currentstep_aa < N_step,

    aa.servoAttach(1);
    % I set the driver with a speed of 12800 Pulse/Rev, so the motor
    % rotates in 256s. With a simple operation i found : For 3.6s =
    % pause(??)= (3.6*256)/360 = 2.56s

    % The driver is set to 12 800 (micro)pulses/revolution
    % The duration of each pulse is 20 ms.
    % So it takes 20 E-3 * 12800 = 256 s to complete a full rotation.
    % The frame_duration (during which the stepper is actioned)for
    % 1/N_step rotation is



    pause(frame_duration)
```

```
    aa.servoDetach(1);
    pause(4)        % pause to insure that the EMF has reached its steady
state

    %%%%%%%%%%%%%%%%%%%%%%%%%%%%%%%%%%%%
    %  CHANNEL 1 ACQUISITION

    % switch channel
    % Allow channel switch
    set(VNA,'EOSMode', 'read&write');
    fopen(VNA);
    % channel switch
    fprintf(VNA,'chan1');
    fclose(VNA);
    % Lock channel switch
    set(VNA,'EOSMode', 'none');

    fopen(VNA);
    % Set data return format and trigger a single measurement
    fwrite(VNA, 'FORM5; OPC?; SING');
    opc_comp=fscanf(VNA);

    % Read data back from analyzer
    %Ask for data
    fwrite(VNA, 'OUTPDATA');
    %Read out #A from binblock
    temp=fread(VNA, 2, 'char');
    %Read out block size
    temp=fread(VNA, 1, 'uint16');
    %Read out trace data
    data_CHAN1_1=fread(VNA, temp/4, 'float32');
    points=temp/(4*2);
    %Allocate space for data array
    data_CHAN1_=zeros(points,2);
    %Reshape output array into two columns
    for i=1:1:points
        data_CHAN1_(i,1)=data_CHAN1_1((2*i)-1);
        data_CHAN1_(i,2)=data_CHAN1_1(2*i);
    end

    fclose(VNA);
    pause(0.5)          % additive pause when changing channel


    %%  CHANNEL 2 ACQUISITION                                          % AC

    % switch channel

    % Allow channel switch
    set(VNA,'EOSMode', 'read&write');
    fopen(VNA);
    % channel switch
    fprintf(VNA,'chan2');
    fclose(VNA);
    % Lock channel switch
    set(VNA,'EOSMode', 'none');

    fopen(VNA);
    % Set data return format and trigger a single measurement
    fwrite(VNA, 'FORM5; OPC?; SING');
    opc_comp=fscanf(VNA);

    % Read data back from analyzer
    %Ask for data
```

```
    fwrite(VNA, 'OUTPDATA');
    %Read out #A from binblock
    temp=fread(VNA, 2, 'char');
    %Read out block size
    temp=fread(VNA, 1, 'uint16');
    %Read out trace data
    data_CHAN2_1=fread(VNA, temp/4, 'float32');
    points=temp/(4*2);

    %Allocate space for data array
    data_CHAN2_=zeros(points,2);
    %Reshape output array into two columns
    for i=1:1:points
        data_CHAN2_(i,1)=data_CHAN2_1((2*i)-1);
        data_CHAN2_(i,2)=data_CHAN2_1(2*i);
    end

    %Calculate the frequency scale
    data_CHAN2_2 = query(VNA, 'POIN?','%s');
    Npoints=str2num(data_CHAN2_2);

    data_CHAN2_3 = query(VNA, 'STAR?');
    Fmin = str2num(data_CHAN2_3);

    data_CHAN2_4 = query(VNA, 'SPAN?');
    Fspan = str2num(data_CHAN2_4);
    Freq = Fmin:Fspan/(Npoints-1):Fmin+Fspan;

    fclose(VNA);

    %Save Process
    magnitudeS11=sqrt(data_CHAN1_(:,1).^2+data_CHAN1_(:,2).^2);
    magnitudeS21=sqrt(data_CHAN2_(:,1).^2+data_CHAN2_(:,2).^2);
    RC=[transpose(Freq) data_CHAN1_ magnitudeS11 data_CHAN2_ magnitudeS21];

    cd('C:\Users\211170836\Desktop\Arduino installation
Pack\Verena\data2004sec');
    save(['Step_MotorHorizontal_' num2str(currentstep_bb)
'Step_MotorVertical_' num2str(currentstep_aa+1) '.txt'],'RC','-ascii');
    currentstep_aa=currentstep_aa+1


end

    currentstep_aa=0;

end
```

## Appendix D: Schematic diagrams

### Micro-stepping driver DQ542MA

Shown in Figure D.1 is a schematic diagram of a complete stepping system. It includes stepping motor, stepping driver, power supply and controller (pulse generator).

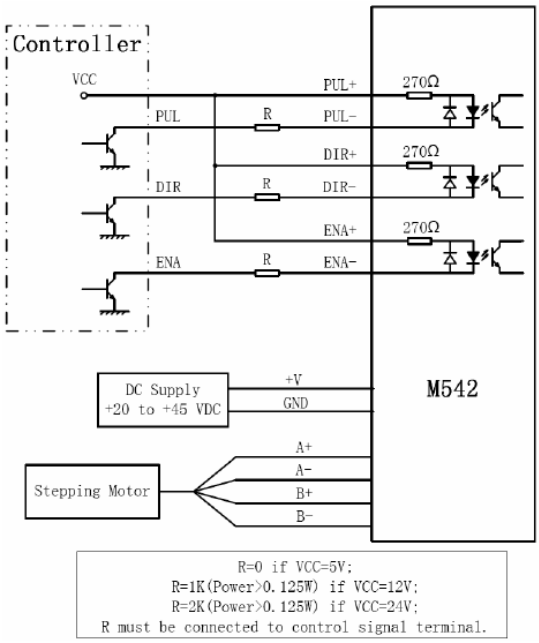


**Figure D.1: Schematic diagram of a typical connection for a micro-stepping driver DQ542MA (Wantai, 2000)**

The RS 535-0445 stepper 4 leads represents; Red – A+, Blue – A-, Black – B- and Green – B+. The controller (Arduino Uno board ATMEGA328P-PU microcontroller) Pin 8 is direction, pin 9 is steps and ground.

## Appendix E: HyperLOG® 7040 – Aaronia antenna's SWR

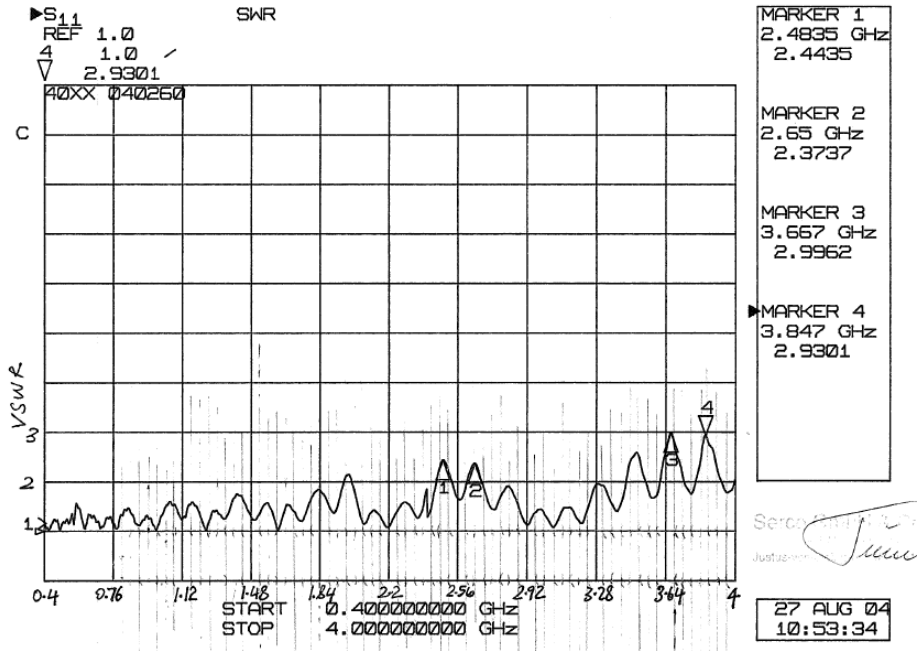


**Figure E.1: VSWR for HyperLOG® 7040 – Aaronia antenna**